Multi-Spectroscopic Investigations for Comprehensive Structural Analysis of Aluminoborosilicate Glasses: I. Integrating Raman, XPS, XAS and NMR Techniques

Hanyu Hu[1] iD, Sami Soudani[1,2] iD, Jonathan Hamon[1], Nicolas Trcera[3] iD, Michael Paris[1] iD, and Yann Morizet[1,2] iD

[1] Nantes Université, CNRS, Institut des Matériaux Jean Rouxel (IMN), 44322 Nantes Cedex, France

[2] Nantes Université, Nantes Atlantique Universités, Laboratoire de Planétologie et Géosciences de Nantes (LPG), UMR CNRS 6112, 44322 Nantes Cedex, France

[3] Synchrotron SOLEIL, L'Orme des Merisiers, Départementale 128, 91190 Saint-Aubin, France

*Correspondence: Yann Morizet, yann.morizet@univ-nantes.fr

Abstract. For relatively simple glasses, such as binary or ternary glass systems, various characterization techniques have proven effective for determining network structures. However, structural analysis of multicomponent glass systems remains challenging due to complex network structures. In this study, we employed Raman, XPS, XAS, and NMR techniques to investigate the structure of soda lime aluminoborosilicate glasses. Our focus was on the polymerization degree of the silicate network (average Q^n value), the content of Non-Bridging Oxygen (NBO%), the connectivity between borate species ($^{[3]}$B-O-$^{[3]}$B% and $^{[3]}$B-O-$^{[4]}$B%), and the chemical environment of Ca and Na cations. Raman spectral decomposition enabled the determination of the polymerization degree of the silicate network, which agreed well with the values calculated from ^{11}B and ^{27}Al NMR spectra for glasses without B-NBO species. XPS O1s spectra decomposition provided consistent NBO content values with those calculated from NMR results. The ^{11}B DQ-SQ NMR spectra can analyse the connectivity changes between borate species across different glass compositions. The ^{23}Na NMR spectra can provide a comprehensive view of the local environment of Na. The XAS spectra provided reliable insights into the local environment of Ca, detailing first shell configurations not easily obtained via NMR. We also presented an analysis scheme for ^{11}B NMR spectra to distinguish between $^{[4]}$B(3Si,1B) and $^{[4]}$B(4Si,0B) species. This study emphasizes the necessity of using a multi-spectroscopic approach to analyse the complex glass network structure.

Keywords: Aluminoborosilicate Glasses, Raman Spectroscopy, XPS Spectroscopy, NMR Spectroscopy, XAS Spectroscopy

1. Introduction

Aluminoborosilicate glasses have gained widespread recognition as materials extensively utilized on a global scale owing to their high chemical and physical stability [1], [2], [3]. Notably, there has been significant progress in the advancement of technical glasses, such as optical fibers for communication purposes [4], [5], [6] and glasses used as matrices for the confinement of nuclear waste [7], [8], [9]. Consequently, the structural analysis of these glasses has emerged as a focal point in the ongoing scientific progression of glass studies, such as the polymerization and depolymerization reactions of silicate networks [10], [11], the

coordination states of boron and aluminum [12], [13], [14], [15], [16] and the influence of alkaline cations [17], [18]. In the past few decades, Raman spectroscopy [19], [20], X-Ray Photoelectron Spectroscopy (XPS) [21], [22], [23], X-ray Absorption Spectroscopy (XAS) [24], [25], [26], [27], [28], [29] and Solid State Nuclear Magnetic Resonance (NMR) spectroscopy [30], [31] have been widely employed for the investigation of glass structures. Due to the inherent disorder evident in the long-range structure of glass, manifested as broad peaks in various spectra, the structural analysis becomes relatively intricate, thereby obscuring valuable information regarding its arrangement. To address this complexity, we aspire to establish a comprehensive structural understanding by synthesizing the advantages and drawbacks of those spectroscopic techniques and constructing a coherent interpretation.

According to Sun's theory [32], oxides in an oxide network glass can be categorized into three distinct classifications. The first category is the network forming oxides (e.g. SiO_2, B_2O_3, GeO_2, P_2O_5) that possess the ability to self-bind through Bridging Oxygen (BO) linkages, often assuming a tetrahedral configuration. The second category is the modifier oxides (e.g. Na_2O, CaO, K_2O, MgO) that play a role as modifiers by disrupting BO linkages and producing Non-Bridging Oxygen (NBO) connections. Alternatively, they act as charge compensators in presence of local positive charge deficits, as observed for tetrahedral boron species ($^{[4]}B$) or tetrahedral aluminium species ($^{[4]}Al$) compared to tetrahedral silicon ($^{[4]}Si$) species. The final category, intermediate oxides like Al_2O_3, Fe_2O_3, ZnO, assume a network-forming position but cannot independently form glass. The network formation process among formers is termed network polymerization, described by the degree of connectivity denoted by Q^n species [33], where n represents the number of BO connected to a silicate tetrahedron: Q^0, Q^1, Q^2, Q^3, Q^4 for silicate glasses (e.g. Q^0 represents an isolated silicate tetrahedron surrounded by four NBOs; Q^4 represents a silicate tetrahedron connected by four BOs). For more complex glass system, such as aluminoborosilicate glasses, the degree of connectivity can be also described more precisely using the nomenclature of $Q^n_{mAl/B}$ [34], where n represents the number of BO connected to a silicate tetrahedron and m represents the number of BO connected to a tetrahedron with aluminate or borate species (e.g. Q^2_{1Al} represents a silicate tetrahedron connected by two BOs, one of which is connected to an aluminate species; Q^4_{4B} represents a silicate tetrahedron connected by four BOs, all of which are connected to borate species). Another way to evaluate the degree of network polymerization is related to the NBO content. Generally, a higher NBO content on Si species indicates lower network polymerization degree. However, it is important to note that according to Dell's model [35], for B-bearing silicate glasses, particularly in highly depolymerized glasses, B species may also contain NBO, which has been confirmed by ^{17}O 3QMAS techniques [15]. The average polymerization can be calculated given the concentration of Q^n species with the following equations that calculate the average *n* value of Q^n units within the glass structure if only considering the presence of Si-NBO within the network:

$$n = 1 \times [Q^1] + 2 \times [Q^2] + 3 \times [Q^3] + 4 \times [Q^4] \qquad (1)$$

$$n = 4 - NBO/Si \qquad (2)$$

where $[Q^n]$ is the relative proportions of Q^n units and the ratio NBO/Si represents the number of NBO per silicate site.

To obtain information about Q^n speciation, various analytical techniques such as ^{29}Si NMR [36], [37], [38], [39], [40], [41], [42], [43], [44] or Raman spectroscopy [45], [46], [47], [48], [49], [50], [51], [52] can be used for the direct identification of silicate tetrahedra, while ^{17}O NMR [53], [54], [55], [56], [57], [58], [59], [60], [61], [62], [63], [64] or O 1s XPS spectroscopy [65], [66], [67] can be utilized to analyze oxygen species (i.e. NBO content). However, a notable challenge arises in the case of ^{29}Si and ^{17}O spectra, given their considerable time consumption due to the low natural abundance of ^{29}Si (4.7%) and ^{17}O (0.04%). Meanwhile, the enrichment of ^{29}Si and ^{17}O isotopes in glasses makes the synthesis very expensive and potentially changes the process of synthesis. It is necessary to use slightly reducing conditions under Ar

gas to avoid exchanges between [17]O of melt and [16]O of the furnace atmosphere for [17]O enriched glass synthesis. At the same time, Raman, and O 1s XPS spectra present challenges as the peaks of different species tend to overlap because the lack of resolution, leading to ongoing controversies in peak deconvolution. Moreover, the literature on the XPS use for determining the glass polymerisation through O 1s analysis is scarce [65], [66], [67]. Because of their respective limitations, using only one method for determining glass structure is insufficient. Until around the last decade, studies combining structural probes with enrichment of [29]Si or [17]O isotope in glasses were not common [34], [38], [50], [68]. Fortunately, after determining the exact glass chemical composition, the quantification of NBO in aluminoborosilicate glasses can be indirectly calculated by examining the quantities of 4-coordinated [4]B and [4]Al species obtained through ^{11}B and ^{27}Al NMR spectra because only [4]B and [4]Al species require charge compensation [15], [35], [69] such as:

$$nNBO = nM^{n+} - n^{[4]}B - n^{[4]}Al \tag{3}$$

where nNBO is the absolute number (atomic number normalized by the composition) of NBO, nM^{n+} is the absolute number of alkaline or/and alkaline-earth ions and $n^{[4]}B$ and $n^{[4]}Al$ is the absolute number of [4]B and [4]Al species calculated based on NMR results and glass chemical composition. Therefore, combining the results obtained by Raman and XPS spectroscopies with the NMR results through the calculation of nNBO and average *n* value of Q^n units is a real opportunity. It is worth noting that, in the present work, the impact of [5]Al and [6]Al species on NBO content calculation has been neglected.

This study investigates four diverse glass composition lines to compare Raman, XPS, XAS and NMR spectroscopic results. The first two series, B15Nay [67] and CxNy [70], have been published recently. The B15Nay composition line is characterized by various ratios of Na/Si, used to understand the influence of Na on the relative content of Si in the silicate network. The CxNy composition line is characterized by various ratios of Ca/Na, used to study the competitive relationship between Ca and Na in the glass network. The second two series, CaNa-RnKp and Ca-RnKp, correspond to two low-polymerisation glass series with different R' and K' values. Since the investigated glass compositions contain Ca and Al, the values of R' and K' are improved based on the Dell model [15], [35], originally developed for ternary alkali borosilicate glasses that do not contain CaO and Al_2O_3, such as:

$$R' = (CaO + Na_2O)/(B_2O_3 + Al_2O_3) \tag{4}$$

$$K' = SiO_2/(B_2O_3 + Al_2O_3) \tag{5}$$

CaNa-RnKp composition line is characterized by a constant ratio of Na/Ca and Ca-RnKp composition line only contains Ca as modifier cation. These two series are designed to understand the role of Na and Ca in highly depolymerized aluminoborosilicate glasses. Therefore, in the present work (Part I), we attempt combining ^{11}B and ^{27}Al NMR results with Raman and XPS spectroscopic results to give a comprehensive interpretation of those techniques. The discussion explores two main aspects: first, based on information from the literature, proposing reasonable methods for peak deconvolution in different spectra. Second, comparing different characterization techniques to understand the effective structural information each can provide and to identify their respective limitations. The impact of compositional variations on the structure of aluminoborosilicate glasses will be addressed in Part II.

2. Experimental methods

2.1 Glass synthesis

The composition of investigated glasses in this work are reported in Table 1. 21 aluminoborosilicate glasses are synthesized in the $CaO-Na_2O-Al_2O_3-B_2O_3-SiO_2$ glass system with 4 different series: (a) CaNa-RnKp series, (b) Ca-RnKp series, (c) CxNy series [70] and (d) B15Nay series [67].

Each glass composition was prepared from a mixture of pure oxides (SiO_2, Al_2O_3, B_2O_3, CaO) and sodium carbonate (Na_2CO_3). The starting materials were carefully mixed in an agate mortar then poured into a Pt crucible. The glasses were synthesized through a process involving the fusion and rapid cooling of initial powders within a platinum crucible including a fusion stage at 1200 °C in a box furnace, maintaining fully oxidizing conditions for one to two hours, followed by immediate quenching in cold water. The recovered glass was scrutinized to check for the presence of crystalline phase under the microscope.

2.2 Glass composition analyses

The major element concentrations for the newly synthesized glasses (CaNa-RnKp and Ca-RnKp) have been determined using Scanning Electron Microscopy with Energy Dispersive Spectrometer (SEM EDS). Glass chips were mounted into epoxy resin plugs polished to 1 µm and followed by carbon coating (25 nm thick). The measurements were conducted on a JEOL JSM 5800LV SEM (IMN Jean Rouxel), equipped with a SDD SAMx dispersive spectrometer. We used the same analytical conditions as previously reported [67], [70]: 15 kV for voltage, 0.5 nA for current, several acquisitions on a 20 µm spot size, acquisition of 60 s. We used corundum for Al_2O_3, wollastonite for SiO_2 and CaO, NaCl for Na_2O as internal standards for quantifying the elements. We obtain an uncertainty on major element measurements better than 5% in relative to the value. Data in mol.% are provided in Table 1 along with the error that is calculated from the standard deviation of the replicated measurements.

Due to its lower molecular mass, the B_2O_3 content is determined using a Laser Ablation-Inductively Coupled Plasma-Mass Spectrometry (LA-ICP-MS, LPG Nantes). The spectrometer is an ArF excimer laser (193 nm, Analyte G2, Photon Machines) that is coupled to a quadrupole ICP-MS (Varian Bruker 820-MS). The ablation is performed in a HelEx II 2-Volume Cell with He as carrier gas. Similarly, we used the same analytical conditions reported in previous studies [67], [70]: laser energy density of 4.54 $J.cm^{-2}$ and with a repetition rate of 10 Hz, five acquisitions in spot mode with a diameter of 110 µm, acquisition time of 30 s preceded and followed by a 30 s blank acquisition and washout time of 30 s.

As shown in Table 1, the calculated R' and K' values of the analysed compositions have changed compared to the nominal ones. For the CaNa-RnKp series, the R' and K' values are higher than the nominal ones, while for the Ca-RnKp series, the R' values are lower, and the K' values are higher than the nominal ones. This may be due to the evaporation of B_2O_3 during the glass synthesis process and the contamination of H_2O in the CaO precursor.

For the reported CxNy series [69], the major element concentrations have been determined using SEM EDS. The uncertainty on element measurements is typically ±0.2 mol.%. For the reported B15Nay series [66], the major element concentrations have been determined using SEM EDS for SiO_2, Al_2O_3 and Na_2O, and using LA-ICP-MS for the quantification of B_2O_3. Error has been determined from the standard deviation calculated from several measurements (at least five acquisitions by SEM EDS and LA-ICP-MS)

Table 1. *Major elements composition of the synthesized soda lime aluminoborosilicate glass series from SEM-EDS measurement and main results deduced from Raman, XPS, XAS and NMR spectra: average n value of Q^n units (Q^n), apparent proportion of $^{[3]}B-O-^{[3]}B$ correlation ($^{[3]}B-O-^{[3]}B\%$), NBO content (NBO%), average distance between Ca and O atoms (r_{Ca-O}), coordination number of neighboring O atoms of Ca (CN_{Ca-O}), chemical shift of ^{23}Na (δ_{Na}), coordination number of Al (CN_{Al}) and proportion of $^{[4]}B$ (N_4). The error bars are reported in between brackets and were estimated by the propagation of uncertainty or estimated from the spectra fitting processes.*

Glass ID	Composition (mol.%)					R'	K'	Raman		XPS	XAS		NMR					
	SiO_2	Al_2O_3	B_2O_3	CaO	Na_2O			Q^n	$^{[3]}B-O-^{[3]}B\%$	NBO%	r_{Ca-O} (Å)	CN_{Ca-O}	δ_{Na} (ppm)	CN_{Al}	N_4	$^{[3]}B-O-^{[3]}B\%$	NBO%	Q^n
CaNa-RnKp																		
CaNa-R2K1	31.8(2)	5.9(1)	12.0(0)	20.1(1)	29.4(2)	2.8	1.8	2.7(1)	55.2	42.6	2.55(28)	5.8(3)	6.5(3)	4.0(1)	0.17(6)	84(6)	50.4(5)	1.3(1)
CaNa-R2K2	49.6(1)	4.6(0)	9.4(0)	15.7(1)	20.8(2)	2.6	3.6	3.1(1)	60.5	32.1	2.66(32)	5.8(4)	1.0(3)	4.0(1)	0.40(6)	64(6)	31.7(4)	2.9(0)
CaNa-R2K3	58.3(3)	3.5(0)	9.6(0)	12.2(2)	16.3(4)	2.2	4.4	3.3(1)	57.7	22.6	2.67(32)	6.4(6)	-3.2(3)	4.0(1)	0.52(6)	52(6)	21.8(3)	3.3(0)
CaNa-R3K2	40.1(1)	4.0(1)	10.1(0)	19.4(2)	25.5(1)	3.2	2.9	2.8(1)	54.6	45.4	2.54(28)	5.7(3)	6.0(3)	4.0(1)	0.22(6)	82(6)	45.7(4)	2.1(1)
CaNa-R3K3	49.5(1)	2.9(1)	8.0(0)	15.8(1)	23.8(2)	3.6	4.5	3.1(1)	49.0	42.0	2.60(29)	5.7(5)	2.6(3)	4.0(1)	0.39(6)	64(6)	39.1(3)	2.6(0)
CaNa-R3K4	57.3(4)	2.9(0)	7.2(0)	13.7(4)	18.9(1)	3.2	5.7	3.3(1)	49.5	25.7	2.66(31)	6.0(4)	-0.5(3)	4.0(1)	0.51(6)	54(6)	29.4(3)	3.1(0)
Ca-RnKp																		
Ca-R2K1	30.3(1)	7.2(1)	18.7(0)	43.6(1)	0.0	1.7	1.2	2.8(1)	55.4	48.3	2.59(28)	5.9(2)	-	4.2(2)	0.21(6)	77(6)	37.2(7)	1.8(2)
Ca-R2K2	46.2(2)	5.7(0)	15.0(0)	32.9(2)	0.0	1.6	2.2	3.0(1)	56.4	47.4	2.65(27)	5.9(2)	-	4.1(2)	0.27(6)	70(6)	25.4(5)	3.0(1)
Ca-R2K3	56.7(2)	4.8(1)	12.5(0)	25.9(2)	0.0	1.5	3.3	3.0(1)	57.8	37.2	2.68(30)	6.0(2)	-	4.1(2)	0.24(6)	75(6)	17.5(4)	3.4(0)

Ca-R3K2	39.7(3)	4.5(1)	12.5(0)	43.1(3)	0.0	2.5	2.3	2.8(1)	56.3	74.1	2.54(26)	5.6(3)	-	4.2(2)	0.24(6)	77(6)	41.9(5)	2.2(1)
Ca-R3K3	48.6(3)	4.0(1)	17(0)	36.6(3)	0.0	2.5	3.3	3.0(1)	50.7	55.9	2.57(28)	5.7(2)	-	4.1(2)	0.26(6)	72(6)	34.0(4)	2.8(0)
Ca-R3K4	56.3(2)	3.7(1)	9.4(0)	30.4(2)	0.0	2.3	4.3	3.1(1)	57.3	n.a.	2.66(30)	5.9(2)	-	4.1(2)	0.24(6)	77(6)	27.3(3)	3.1(0)
CxNy																		
C35N0	32.4(2)	4.9(2)	29.1(2)	33.6(2)	0.0	1.0	1.0	2.9(1)	37.5	n.a.	n.a.	n.a.	-	4.1(2)	0.33(6)	n.a.	19.1(9)	2.8(3)
C30N5	31.9(2)	5.2(2)	29.7(2)	28.4(2)	5.0(2)	1.0	0.9	3.0(1)	48.4	n.a.	n.a.	n.a.	-7.7(3)	4.1(2)	0.35(6)	n.a.	17.6(9)	2.9(4)
C20N15	33.9(2)	5.0(2)	29.0(2)	17.9(2)	14.3(2)	1.0	1.0	3.1(1)	40.0	n.a.	n.a.	n.a.	-3.6(3)	4.0(1)	0.41(6)	n.a.	15.2(9)	3.1(3)
C10N25	32.9(2)	4.9(2)	29.6(2)	8.9(2)	23.6(2)	0.9	1.0	3.2(1)	55.4	n.a.	n.a.	n.a.	-0.6(3)	4.0(1)	0.44(6)	n.a.	14.5(9)	3.1(3)
C0N35	31.5(2)	5.3(2)	37.0(2)	0.0	32.5(2)	0.9	0.9	3.4(1)	56.0	n.a.	n.a.	n.a.	1.3(3)	4.0(1)	0.53(6)	n.a.	10.7(9)	3.3(4)
B15Nay																		
B15Na10	64.8(1)	5.9(1)	18.0(1)	0.0	11.3(1)	0.5	2.7	3.7(1)	50.0	1.8	n.a.	n.a.	-12.4(3)	4.0(1)	0.36(6)	81(6)	0	4.0(0)
B15Na20	63.2(1)	4.2(0)	14.9(1)	0.0	17.7(0)	0.9	3.3	3.5(1)	71.9	2.9	n.a.	n.a.	-6.5(3)	4.0(1)	0.65(6)	30(6)	3.8(4)	3.9(0)
B15Na30	51.8(0)	4.8(1)	14.8(0)	0.0	28.5(0)	1.4	2.6	3.4(1)	73.9	34.1	n.a.	n.a.	-0.5(3)	4.0(1)	0.61(6)	28(6)	15.4(5)	3.4(1)
B15Na40	44.7(1)	6.5(0)	13.9(0)	0.0	34.9(2)	1.7	2.2	3.0(1)	54.5	48.4	n.a.	n.a.	3.4(3)	4.0(1)	0.37(6)	58(6)	25.1(5)	3.0(1)

R' and K' were calculated by Eq. 4 and 5 on the main text.

n.a.: not analyzed.

2.3 Raman spectroscopy

The Raman spectra were acquired on several glass chips of each sample at the LPG. We used a Jobin-Yvon LabRam HR800 equipped with a solid-state laser operating at 532 nm. We set the output power at 100 mW and we did not observe any damage on the glass sample at this power. We used a grating of 1800 grooves/mm corresponding to a spectral resolution of 0.5-0.8 cm^{-1}. The Raman acquisitions were conducted in non-confocal mode (slit aperture = 200 µm) to obtain the maximum of signal. We used a X50 Olympus long working distance objective. With this configuration, the spot size is ~1 µm in diameter and the analysed depth on the order of ~10 µm. The spectral region analysed ranges from 250 to 1800 cm^{-1} covering the symmetric stretch vibrations of the silicate units (850-1250 cm^{-1}) and the symmetric stretch of the trigonal boron units (1350-1550 cm^{-1}). We collected 4 spectra on each sample and four different glass chips. The acquisition time was set to 30 and 45 s and 10 scans. Each Raman spectrum was treated with Labspec 6.5© software for background removal with a fourth order polynomial function and for peak area determination. The obtained spectra were subsequently treated with Origin2019© software for normalizing to the highest intensity and fitting the symmetric stretch areas. We used four to five Gaussian functions for the silicate stretching region and two to three Gaussian functions for the trigonal boron stretching region. The way spectra were fitted is as follow: 1) the Gaussian peak initial positions were fixed according to literature data (see details in Table S1) at 870 (if required), 930, 1020, 1080, 1180, 1370 (if required), 1400 and 1500 cm^{-1}, 2) the peak FWHM (Full Width at Half Maximum) is set to 70 cm^{-1} initially for all Gaussian peaks except for the peak at 870 cm^{-1} that clearly exhibits a lower peak width and is fixed at 30 cm^{-1}, 3) the peak positions and areas are optimized conjointly at fixed FWHM, 4) the FWHM of each peak is then optimized at fixed peak position. The four steps are repeated several times until the χ^2 corresponding to a figure of robustness is not evolving upon fitting. The attribution of each Gaussian peak will be discussed later in the manuscript.

2.4 XPS spectroscopy

The acquisition of the XPS spectra was conducted using the same protocol as previously reported [67], [70]. We obtained the XPS spectrum on each glass sample for O and Si environments. The XPS analyses were carried out on a Kratos Nova spectrometer (IMN Jean Rouxel) using a monochromatic Al Kα radiation operating at 1486.6 eV (15 kV, 20 mA) and using the neutralization of the sample surface (i.e. glasses are insulating). We analysed glass chips (several mm^2) corresponding to a surface fracture from the bulk of the experimental charge. The surfaces were not prepared and the analyses were conducted on raw glass surfaces, hence avoiding possible surface contamination. However, the analysed glass surface has been obtained well before the XPS analysis. The glass chips were loaded into the sample chamber under high-vacuum conditions (<10^{-8} mbar). The spot size on the sample is 300x700 µm^2 area. We recorded survey spectra at a pass energy of 160 eV corresponding to an overall instrument resolution of 1.95 eV and a step of 0.5 eV from -5 to 1200 eV. High-resolution spectra of O 1s, Si 2p and C 1s core levels were recorded. The instrumental resolution was determined to be 0.54 eV at a pass energy of 40 eV using the Fermi edge of the valence band for metallic silver. We used an energy step of 0.1 eV. We acquired the final spectrum with a cycling mode (10 scans on each sample) for each element and we did not observe any modification of each individual acquisition that would suggest an alteration of the glass under the X-ray beam. We calibrated the XPS spectra using the adventitious C 1s in the binding energy at 284.8 eV.

The spectra were treated with CasaXPS© software [71]. The Si 2p peak was fitted with two Gaussian-Lorentzian functions accounting for the Si 2p$_{1/2}$ and 2p$_{3/2}$ contributions separated by 0.61 eV and with a peak area of 2/3 and 1/3, respectively. The peak position and FWHM were left free to evolve during the fit. For the O 1s XPS peak, we have considered that the glass structure can be represented by two types of BOs and two types of NBOs. A detailed discussion is proposed later on in the manuscript. We used the same optimization method as described in Morizet et al. [67] and based on previous literature data (see Table S3). We took

into consideration several aspects: FWHM is identical for peaks of identical oxygen type; BOs are located at higher binding energy than NBOs; BOs has higher FWHM than NBOs; B-bearing oxygen species have higher binding energy than Si-bearing oxygen species. We firstly optimized the position of the BOs peak followed by the position optimization of the NBOs peak. We conducted the same approach for the peak FWHM. For Na-bearing glasses (i.e. CaNa-RnKp), we added an additional peak accounting for the Na KLL Auger peak at ~536 eV. For B15Nay glasses, we used the data reported in Morizet et al. [67]. The entire set of fitting parameters can be found in the Suppl. Mat. in Table S4. We did not characterize the Si 2p and O 1s environments for CxNy glasses.

2.5 XAS spectroscopy

Ca K-edge XAS spectra were collected on LUCIA beamline at SOLEIL synchrotron [72], [73] using a double Si(111) monochromator. The acquisitions were conducted in the X-ray Absorption Near-Edge Spectroscopy (XANES) and the Extended X-ray Absorption Fine Spectroscopy (EXAFS) regions. The glass spectra were acquired in the fluorescence mode by using a silicon drift diode detector Bruker with an active surface of 60 mm^2. The energy calibration was achieved with a Ti foil at a K-edge of 4966 eV. The incoming beam size was 3×5 mm^2. The sample powders were stuck onto a carbon rubber on a copper plate. The sample orientation had a 4° angle normal to the detector in order to have a configuration where we had the best signal to noise ratio (optimized for collecting the most intense sample signal) and to minimize the possible self-absorption effect. With this configuration, we did not observe any self-absorption as seen from the Athena Self-Absorption implemented tool [74] and did not have to correct the collected spectra. The Ca K-edge spectra were collected in the energy range 3970-4040, 4040-4070, 4070-4125, 4125-4500, 4502-4700 eV with a 2.0, 0.2, 0.5, 1.0 and 2.0 eV step, respectively. We collected at least two spectra, which were averaged using Athena software. The counting time for each point was set to at least 1 second, which is sufficient given the Ca concentrations in several glasses (up to 45 mol.%). The obtained XAS spectra were prepared for analysis using Athena software through the classical procedure [28], [74]. This involved normalizing the spectra by determining the pre-edge and post-edge regions and performing background subtraction using the spline to extract the EXAFS signal.

The simulation of the EXAFS was accomplished using the Artemis software [74]. We used the spectrum obtained on crystalline CaO associated with the corresponding crystalline CaO structure to determine the scattering amplitude S_0^2 at 0.702 and the correction for the edge position ΔE_0 = -4.88 eV. With these parameters, it is possible to determine the Ca first sphere of coordination: coordination number to oxygen atoms and distance to first nearest neighbour. For the Ca EXAFS analysis, we used the k^1 and k^2 weighted data and ranging from 2 to 10 Å^{-1}. The absolute magnitude ($\left|\chi(R)\right|$) of the Radial Distribution Function (RDF in Å) has been fitted in the 1.15 to 3.15 Å region that probes the first coordination sphere but also the second nearest neighbour to some extent. We used one Ca to O single scattering path taken from the CaO crystallographic structure from the Materials Project [75] with r_{Ca-O} = 2.44 Å. However, considering that there are several oxygen types within the glass: BOs and NBOs; we choose to describe the Ca to O single scattering path with three different bond lengths with initial Δr values at -0.15, 0 and +0.15 Å as compared to the initial r_{Ca-O}. Nevertheless, we choose to consider one shared oxygen coordination number (CN_{Ca-O}) for the three Ca to O single scattering paths. Considering the range in the RDF up to 3.15 Å, we had to add a single scattering path corresponding to the second nearest neighbour to the Ca atoms within the glass structure. The possible candidates are Si, B and Al, however, in the investigated CaNa- and Ca-RnKp glasses Si atoms are the most likely present in the Ca surrounding because SiO$_2$ is the most concentrated oxide and it is expected to be in the surrounding of Ca atoms from the statistical viewpoint. Hence, we added a single scattering path Ca to Si taken from the CaAl$_2$Si$_2$O$_8$ (anorthite) crystallographic structure from the Materials Project [76] with $r_{Ca..Si}$ = 3.274 Å.

The initial parametrization for fitting the RDF is as follow: the Debye-Waller attenuation factor (σ_{Ca-i}) is initially set to 0.003. The Ca coordination number to O (CN_{Ca-O}) is set to 6 that is in agreement with our current knowledge on the local environment of Ca in various type of glass compositions [26], [77], [78]. The Ca coordination number to Si ($CN_{Ca..Si}$) has been set to 2 initially, however this parameter is highly uncertain and speculative. The fit of the RDF region of interest has been performed with the following steps: 1) the $r_{Ca-O1,2,3}$ and $r_{Ca..Si}$ are optimized conjointly with fixed σ and CN, 2) the $\sigma_{Ca-O1,2,3}$ and $\sigma_{Ca..Si}$ with fixed $r_{Ca-O1,2,3}$, $r_{Ca..Si}$ and CN, 3) these two steps are repeated several times, 4) the CN_{Ca-O} and $CN_{Ca..Si}$ are optimized at fixed r and σ and 5) the whole process is repeated several times until obtaining a satisfactory fit of the RDF region between 1.15 and 3.15 Å.

2.6 NMR spectroscopy

The MAS-NMR experiments were performed on a Bruker Avance III 500 MHz spectrometer using a 2.5-mm probe. The MAS frequencies (v_{rot}) are 30, 20 and 20 kHz for [23]Na, [27]Al and [11]B nuclei, respectively. The 1D ^{23}Na MAS-NMR spectra were recorded at 132.3 MHz with 3 µs pulse length (corresponding to a π/8 flip angle) at radiofrequency (rf) field of 20 kHz, 1200 transients, and a repetition delay (rd) of 1 s. The 1D ^{27}Al MAS-NMR spectra were recorded at 130.3 MHz with 2 µs pulse length (corresponding to a π/12 flip angle) at rf of 20 kHz, 2048 transients, and a rd of 1 s. The 1D ^{11}B MAS-NMR spectra were recorded at 160.5 MHz with 2.1 µs pulse length (corresponding to a π/12 flip angle) at rf of 20 kHz, 512 transients, and a rd of 5 s. All the rd values were optimized to make sure the experiments are quantitative. The [23]Na, [27]Al and [11]B chemical shifts were referred to NaNO$_3$, Al(NO$_3$)$_3$ solutions at 0 ppm and H$_3$BO$_3$ solutions at 19.6 ppm. The [11]B Spin-Echo (SE) experiments were investigated at v_{rot} = 20 kHz with the Hahn-Echo NMR sequence [79]. The spectra were recorded with a π pulse length of 6.3 µs at a rf of 20 kHz. The echo delay was set to 0.05, 25 and 75 ms with a rd of 5 s. The triple-quantum [11]B (3QMAS) spectra were acquired at v_{rot} = 20 kHz using a four pulses sequence including Z-filter. The Z-filter delay was set to 10 µs. The optimized length of the 3Q-excitation was 3.9 µs for a rf field of 140 kHz. For 3Q-reconversion, we used a 12.5 µs (1/4 of the MAS period) divergent DFS (Double Frequency Sweep) pulse from 100 KHz to 1.5 MHz using a rf of 130 kHz [80]. About 64 t_1 increments of 50 µs were collected with a rd of 1 s. The [11]B/[11]B correlations were investigated at v_{rot} = 20 kHz with the [11]B DQ-SQ (Single Quantum – Double Quantum) NMR sequence [81], [82]. The homonuclear dipolar interaction was reintroduced with the application of a short 2 × 400 µs (excitation/reconversion) BR2$_2^1$ pulse scheme [82] made of π pulse length of 50 µs at a rf of 10 kHz (i.e. ½ v_{rot}). In order to eliminate DQ coherences involving a single nucleus, a π selective pulse of 8 µs sandwiched by two τ intervals of 21 µs (to ensure rotor synchronization [81]) was used during DQ evolution. 64 slices in the indirect dimension were acquired. rd was set to 3 s.

3. Results

3.1 Raman spectroscopy

According to the literature, two spectral regions can be separated and utilized to analyse the structure of borosilicate glass: 800-1250 cm^{-1} region which correspond to the silicate network stretching vibrations (v_{Si-O}) [20], [45], [48], [49], [68] and 1300-1600 cm^{-1} region which correspond to the borate stretching vibrations (v_{B-O}) [27], [28]. This broad silicate peak can be sequentially divided from low to high energies into Q^1, Q^2, Q^3, Q^4 silicate species, although for the precise positions of each peak, no consensus has ever been reached, especially the contribution of Q^4 sites (see Table S1 in the Suppl. Mat., presenting the peak assignment for (boro-)silicate glasses and melts reported in recent literature). For the borate peak, according to the literature, it can be divided from low to high frequency into [3]B-O-[4]B (i.e. [3]B species connected to at least one [4]B species) and [3]B-O-[3]B (i.e. [3]B species connected to at least one [3]B species) species [21], [23], [48], [49], [50]. To minimize the number of figures in the main text, only examples of representative fits are included in the main text. The entire set of

Raman spectra for our investigated $CaO-Na_2O-Al_2O_3-B_2O_3-SiO_2$ glasses can be found in the Suppl. Mat. shown in Figure S1.

Combining peak assignment parameters from the literature, after multiple rounds of fitting and cross-comparison of our samples, we successfully identified five peaks within the silicate network region. Examples of Raman spectra deconvolution are presented in Figure 1. As mentioned previously, there are up to 7 Gaussian individual components denoted S1 to S5 for silicate peaks, B1 and B2 for borate peaks as presented in Figure 1D. Regarding the assignment of these peaks, the first three peaks S1, S2 and S3 generally correspond to Q^1, Q^2 and Q^3 silicate sites, respectively, consistent with findings in the literature [38], [50], [51]. However, the range from 1000 to 1200 cm^{-1} needed to be divided into two peaks (S4 and S5). In pure SiO_2 glass, the Q^4 peak has been previously assigned to two peaks: 1060 and 1200 cm^{-1}, which correspond to transverse optical (TO) and longitudinal optical (LO) modes of an asymmetric stretch of Q^4 BO atoms [49], [51], respectively. Therefore, we retained two Gaussian peaks (S4 and S5) to fit the contribution of Q^4. It is worth noting that recent studies on silicate glasses containing Na [19] and Ba [38], [83] have attributed the peak at 1050 cm^{-1} to the Q^3 Si-NBO stretch vibration, which differs from our peak assignment. However, for aluminoborosilicate glasses, the shift of Q^n towards lower energy, as observed in ^{29}Si NMR spectra [84], is reasonable due to the linkage of silicate sites with B or Al next nearest unit as $Q^n_{mB/Al}$ species [34]. For example, in the case of B15Na10 glass, according to the model of Dell et al. [35], since the Na content is less than the sum of Al and B content, all silicate sites should be in Q^4 configuration. However, the Raman spectrum of B15Na10 glass exhibits a strong signal at 1050 cm^{-1}, making it unreasonable to assign this peak to Q^3 site in aluminoborosilicate glasses. After the deconvolution of Raman spectra, the derived apparent proportion of Q^n species of each sample presented in Table 1 for the calculation of apparent average *n* value of Q^n units (Eq. 1) and then is compared with the calculated average *n* value of Q^n units from NMR results (see Section 4.1.1). It is very important to note that our Raman peak assignment represents one of possible solutions for estimating the apparent average *n* value of Q^n units for multi-former silicate glass systems based on the minimum components fitting processes.

For the higher frequency range (1300–1600 cm^{-1}), two peaks were recognized in borate network region as presented in Figure 1. These two peaks B1 and B2 are consistent with previous literature [48], [49], [50], corresponding to $^{[3]}B-O-^{[4]}B$ and $^{[3]}B-O-^{[3]}B$ species, respectively. The derived ratio of $^{[3]}B-O-^{[3]}B$ to the sum of $^{[3]}B-O-^{[3]}B$ and $^{[3]}B-O-^{[4]}B$ (denoted as $^{[3]}B-O-^{[3]}B\%$) from Raman spectroscopy are presented in Table 1 and are compared with ^{11}B DQ-SQ NMR results in Section 4.1.3.
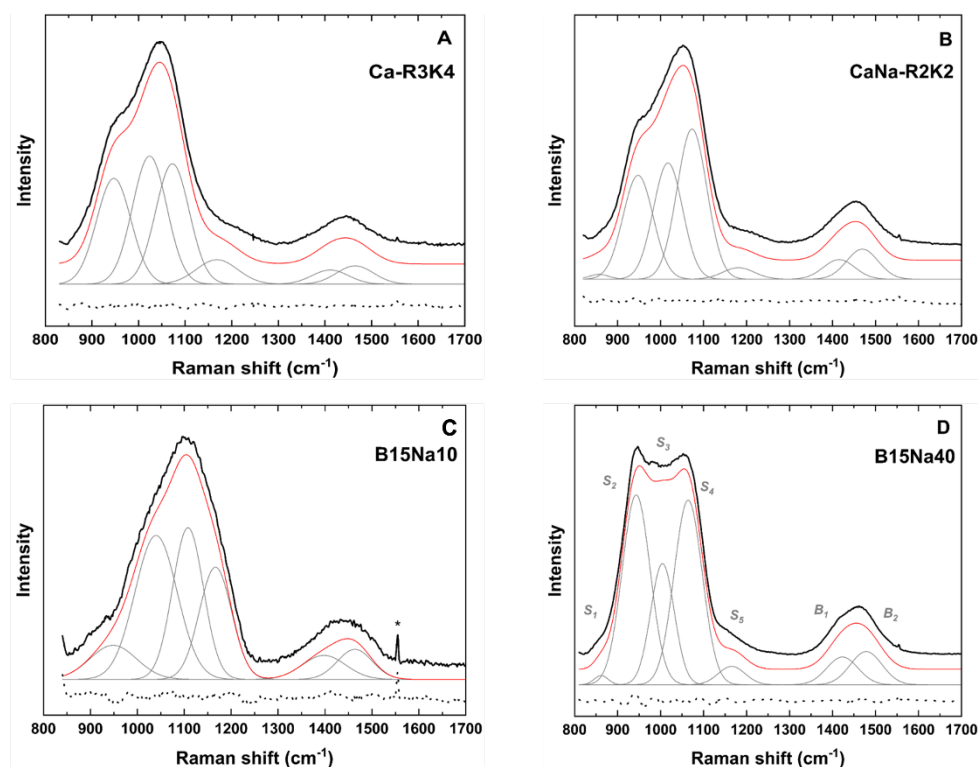
Figure 1. *Examples of Raman spectra (in black) and the associated fit (in red) of Ca-R3K4 (A), CaNa-R2K2 (B), B15Na10 (C) and B15N40 (D) glasses. S1 to S5 represent peaks corresponding to silicate sites, while B1 and B2 denote peaks related to the correlation between borate species. The sharp peak at 1560 cm^{-1} is an artefact corresponding to possible adsorbed H$_2$O onto the sample surface. The residual from the fit is also reported (dotted line at bottom).*

3.2 XPS spectroscopy

Examples of O 1s XPS spectra for the investigated glasses (A. Ca-R2K1; B. Ca-R2K2; C. CaNa-R2K2 and D. CaNa-R2K3) are illustrated in Figure 2. The entire set of spectra and fit parameters can be found in Suppl. Mat. (Figure S2 and Table S4). As mentioned earlier, the presence of the Na KLL Auger line at ~536 eV for Na-bearing glasses was observed. A broad peak ranging from 534 to 528 eV constitutes the oxygen signal in the glass network (BO and NBO). Previous studies have reported that pure SiO$_2$ glass manifests a single peak at 533.2 eV with a FWHM (Full Width at Half Maximum) of 1.25 eV. Upon the introduction of Na$_2$O content, a distinct peak emerges at a lower band energy (B.E., 530 eV), and its intensity steadily increases with Na$_2$O content [66]. Hence, as commonly observed in literature (see Table S3), the prominent O 1s peak can be divided into at least two regions: the binding energy ranging from 533 to 531 eV corresponds to the contribution from BO whereas the binding energy range of 530 to 529 eV indicates the contribution from NBO. The simulations shown in Figure 2 were conducted based on previous description by Morizet et al. [67] for B15Nay glass series samples. In agreement with this approach, we divided the O 1s XPS spectrum into 4 Gaussian-Lorentzian peaks. Taking into account, the mixing of multiple subnetworks species (e.g. Si-O-Si/B/Al, B-O-B) as well as the potential presence of various types of NBO (Si/B-O...Na$^+$/Ca^{2+}) would be too speculative to be determined. The derived concentration of NBO (NBO%) of each sample are presented in Table 1 and will be used for comparison with the calculated NBO% from NMR results in Section 4.1.2.
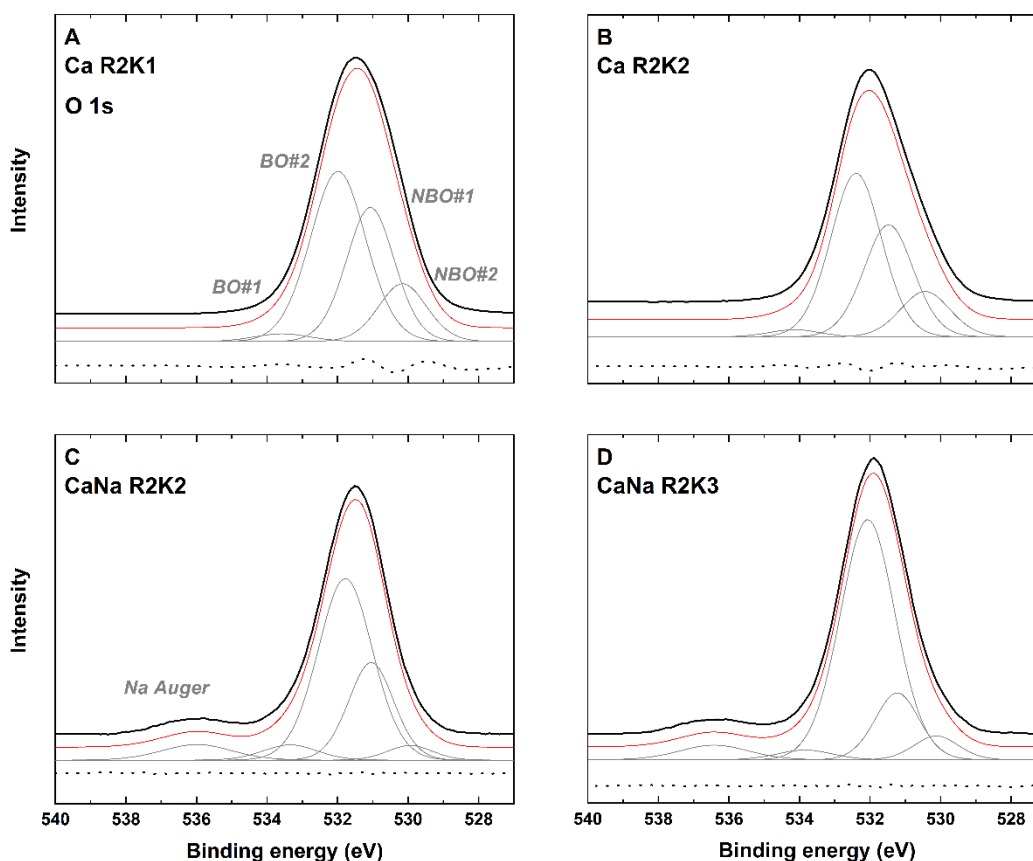
Figure 2. *Examples of XPS O1s spectra (in black) and the associated fit (in red) for Ca-R2K1 (A), Ca-R2K2 (B), CaNa-R2K2 (C) and CaNa-R2K3 glasses. The spectra are fitted with two peaks for BO species and two peaks for NBO species. In addition, for Na-bearing glasses, there is a peak at 536 eV corresponding to the Na Auger line. The residual from the fit is also reported (dotted line at bottom).*

3.3 Ca K-edge XAS spectroscopy

The typical Ca K-edge EXAFS spectra obtained for various glasses are shown in Figure 3 (A. CaNa-R3K4; B. Ca-R3K4; C. CaNa-R2K1 and D. Ca-R2K1), including the RDF fitted region and an insert showing the fit of the imaginary part of the EXAFS function. The remaining spectra can also be found in the Suppl. Mat. (Figure S3). It should be emphasized that the peak observed at ~1.1 Å is ascribed to a beamline artefact because this peak would correspond to a very short bond between Ca and another element at ~1.6 Å. Indeed, there is no known inorganic compound with a structure that features such low bond length involving Ca [85]. For inorganic materials, in particular Ca-bearing silicate glasses, previous studies proposed Ca to O bond length on the order of ~2.5 Å and coordination number to oxygen that can range from 5 to 8 [86]. The fit results (avg. r_{Ca-O} and CN_{Ca-O}) are shown in Table 1 along with the error bars on the derived parameters obtained from Artemis software. The entire set of parameters ($r_{Ca-O\#1, \#2, \#3}$ and $\sigma_{Ca-O\#1, \#2, \#3}$) are provided in the Suppl. Mat. in Table S5. The values obtained (avg. r_{Ca-O} and CN_{Ca-O}) are indicated on each plot in Figure 3. The results align with previous studies [28], showing an average r_{Ca-O} bond length of approximately 2.5 Å and a CN_{Ca-O} near 6. The average $r_{Ca..Si}$ is longer than the average r_{Ca-O}, around 3.4 Å, with a $CN_{Ca..Si}$ about 2. These findings were also corroborated by recent research in SiO_2-Al_2O_3-CaO-MgO slags system conducted by Le Cornec et al. [25]. It is worth mentioning that the quality of the fit is observed to be better in glasses containing only Ca, compared to those containing both Ca and Na. Currently, the reason for this behaviour is not entirely clear, though it might be influenced by the presence of mixed alkali and alkaline-earth cations effect. Previous studies

based on soda-lime silicate glasses have demonstrated the presence of Na-Ca mixing using Molecular Dynamics (MD) simulations [86] and ^{17}O 3QMAS NMR methods [87]. As well as the enhancement of mobility of Ca^{2+} [88] and potential reduction in the quantity of small-membered rings [86], [89] induced by the presence of Na^+ could amplify the multiplicity of Ca^{2+} environments within glass structure. This could explain the difficulty in obtaining a suitable fit and could also explain the larger error obtained on the fit parameters for this particular glass series.
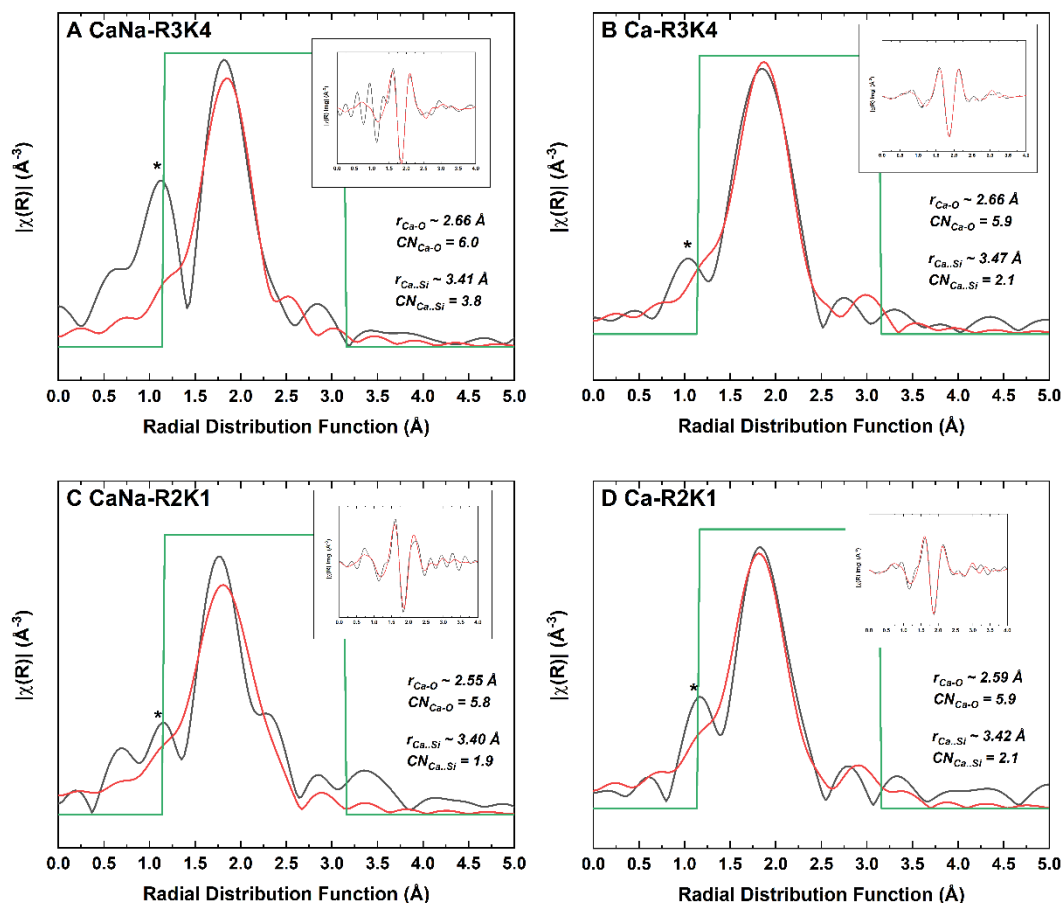
Figure 3. *Examples of K-edge FT-EXAFS spectra in R-space (main window) for various glasses: CaNa-R3K4 (A), Ca-R3K4 (B), CaNa-R2K1 (C) and Ca-R2K1 (D). The red line corresponds to the fit of the spectra in a particular region delimited in green. We also provide the fit of the spectra for the imaginary part of the Fourier transform (inset). The peak indicated by a * is an artefact from the beamline and does not correspond to an actual signal of the Ca environment. The derived average values for r_{Ca-O} and CN_{Ca-O} are also indicated.*

3.4 NMR spectroscopy

The 1D ^{23}Na MAS-NMR spectra along with their fitting examples are presented in Figure 4A, all displaying an asymmetrical peak attributed to the effect of the Electric Field Gradient (EFG) distribution on quadrupolar nuclei. Fits were performed by using the "*Czsimple*" model implemented in the *Dmfit* program [90]. This model integrates a Gaussian distribution of isotropic chemical shift in addition to the EFG distribution. According to previous studies [91], [92], [93], the isotropic chemical shift of [23]Na (δ_{Na}) in sodium silicate and sodium aluminosilicate glasses is primarily influenced by the first neighbour anion effect, represented by the coordination number of Na (CN_{Na-O}) and the first shell distance (r_{Na-O}). A general trend of decreasing δ_{Na} is observed with increasing CN_{Na} and r_{Na-O}. Additionally, it can be affected by

the first neighbour cation effect, represented by the bulk polymerization degree of silicate glass network Q^n. δ_{Na} decreases as the average Q^n value decreases. Thus, the role of Na can be inferred from the δ_{Na} value, where sodium as a charge compensator (bridging oxygen sodium, Na-BO) exhibits a longer r_{Na-O} and is associated with a higher Q^n silicate site compared to sodium as a network modifier (non-bridging oxygen associated with a sodium atom, Na-NBO), which has a shorter r_{Na-O} and is close to a lower Q^n silicate site.
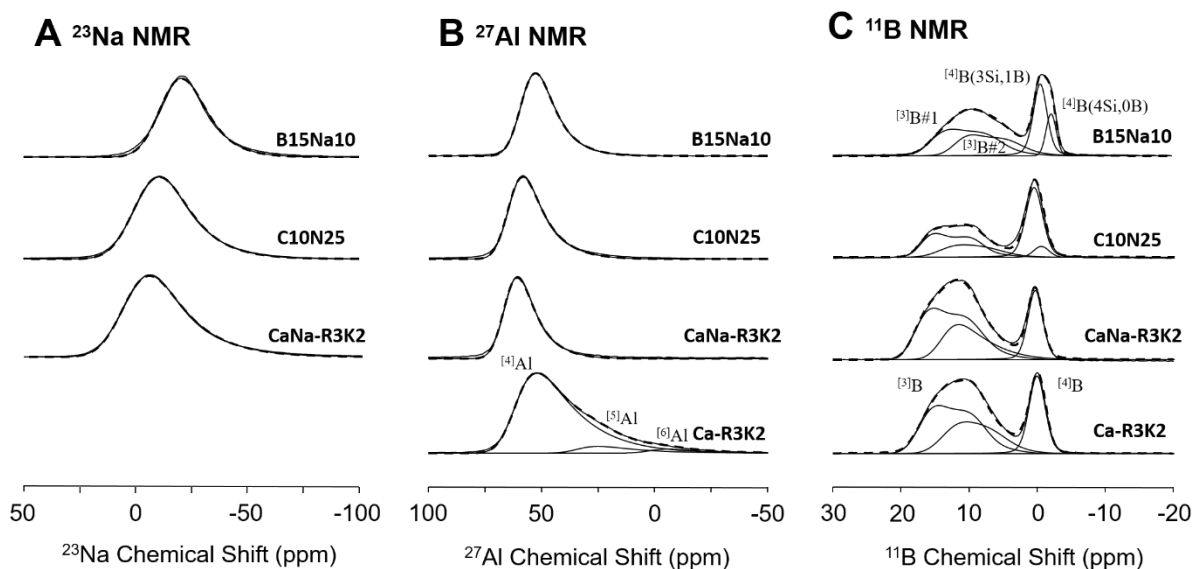
Figure 4. *Examples of 1D ^{23}Na (A), ^{27}Al (B) and ^{11}B (C) MAS-NMR spectra for Ca-R3K2, CaNa-R3K2, C10N25 and B15N10 glasses. The fit of the spectra is provided as a dashed line. We observed one line for ^{23}Na spectra; one to three lines for ^{27}Al spectra representing four-, five- and six-coordinated Al species; two lines for reproducing BO$_3$ species and two lines for BO$_4$ species.*

All the spectra and main fit parameters are shown in the Suppl. Mat. as Figure S4 and Table S6, respectively, which include the isotropic chemical shift (δ_{Na}), the full width at half maximum (FWHM) of isotropic chemical shift distribution and quadrupolar coupling constant (CQ$_{Na}$). The chemical shift shows significant variation ranging from -12 to 6 ppm, while the CQ varies from 2.5 to 3.3 MHz. This variation indicates a notable shift in the main role of Na$^+$ from charge compensator to a network modifier across our investigated glass series (Figure S4). For the CaNa-RnKp series (Figure S4A), the δ_{Na} shifts to lower frequencies as the K' value increases (increase of SiO$_2$ content). In the CxNy series (Figure S4B), the δ_{Na} also shifts to lower frequencies as the Na is replaced by Ca. For the B15Nay series (Figure S4C), the δ_{Na} shifts to higher frequencies as the Na content increases. It is important to note that the ^{23}Na spectrum does not quantify the ratio between the two roles, as it combines contributions from various Na$^+$ environments in the analysed glass without distinguishing between potential different environments. The derived δ_{Na} values of each sample (as presented in Table 1) will be used for comparison with the Ca^{2+} environment from XAS results in the subsequent section.

The 1D ^{27}Al MAS-NMR spectra are given in Figure S5 in the Suppl. Mat. and their fitting examples are presented in Figure 4B. As ^{23}Na spectra, all ^{27}Al spectra exhibit asymmetrical shapes and were fitted using the "*Czsimple*" model. In low Ca-containing glass (i.e. B15Nay, CaNa-RnKp glass series), a single peak near 60 ppm is observed, corresponding to the 4-coordinated aluminate species ($^{[4]}$Al) [94]. Conversely, in samples with a high quantity of alkaline-earth ions (i.e. Ca-RnKp glass series), additional peaks corresponding to 5-coordinated aluminate species $^{[5]}$Al (30 ppm [94]) and even 6-coordinated aluminate species $^{[6]}$Al (0 ppm [94]) are detected. However, these peaks tend to overlap due to the large FWHM values and quadrupolar effect, a phenomenon reported in several studies [68], [95], [96], [97], [98], [99]. Thus, ^{27}Al 3Q-MAS NMR is required to determine the parameters of $^{[5]}$Al and $^{[6]}$Al species and to differentiate between them [68], [97], [98]. Two examples of ^{27}Al 3Q-MAS NMR

maps are provided in the Suppl. Mat. Figure S6. The fit data for [4]Al species including the isotropic chemical shift (δ_{Al}), the full width at half maximum (FWHM) of isotropic chemical shift distribution, the quadrupolar coupling constant (CQ_{Al}) and proportions are tabulated in Table S6. The proportion of [4]Al species will be used for the calculation of NBO content (Eq. 3) [69]. Notably, the chemical shift of ^{27}Al in [4]Al species exhibits a slight variation within the range of 60 to 68 ppm, as marked in Figure S5. According to the literature, the value ^{27}Al chemical shift also depends on the Si-O-Al angle, which is influenced by connected Q^n sites [94]. Similar phenomenon has been observed in $CaO-Al_2O_3-SiO_2$ glass system that the evolution of δ_{Al} values is inversely correlated to the evolution of band frequencies of Q^n species in Raman spectra [68]. Angeli et al. [100] has reported the value of Al-O-Si angle from 147° within most highly polymerized glass to 135° within the most depolymerized glass in $CaO-Na_2O-Al_2O_3-SiO_2$ glass system. Hence, ^{27}Al chemical shift of [4]Al species could potentially serve as an indicator of the average Q^n of silicate network, assuming other bonds such as Al-O-Al or Al-O-B are absent in the glass network. For our investigated glasses, those kinds of bonds are not expected due to the low aluminium content.

The 1D ^{11}B MAS-NMR spectra are given in Figure S7 in the Suppl. Mat. and their fitting examples are presented in Figure 4C, revealing two distinct spectral regions: the one ranging from 20 to 0 ppm corresponds to 3-coordinated borate species ([3]B), while the other, ranging from 0 to -5 ppm, corresponds to 4-coordinated borate species ([4]B) [15], [101]. Nevertheless, in the samples containing a high amount of [3]B species (i.e. B15Na10 glass), these two regions share an overlapping area, leading to uncertainty in the determination of N_4 corresponding to the proportion of [4]B on total B species such as: [[4]B] / ([[4]B] + [[3]B]). Furthermore, the separation of various [3]B and [4]B species proves challenging in MAS-NMR spectra at 11.7 T because of the large CQ values of [3]B species. Consequently, several additional NMR sequences, including ^{11}B 3Q-MAS NMR and ^{11}B DQ-SQ NMR, are used to facilitate the deconvolution of ^{11}B MAS-NMR spectra and determine the different borates species in the glass network.

Firstly, the technique of ^{11}B 3Q-MAS NMR is utilized to distinguish between various [3]B species. An illustrative example of the ^{11}B 3Q-MAS ([3]B part) NMR spectrum and its corresponding fit using "*Amorphous*" model implemented in the *Dmfit* program [90] for the B15Na10 (i.e. the highest SiO_2 content: 64.8 mol.%) and CaNa-R2K1 (i.e. the lowest Si content: 31.8 mol.%) glasses are presented in Figure S8A and S8B, respectively. This model integrates a Gaussian distribution of isotropic chemical shift, quadrupolar coupling constant and the asymmetry parameter, which has been proved effective in modelling this region, despite the lack of a true physical meaning [16], [50], [102]. For the B15Na10 glass, through the fit of ^{11}B 3Q-MAS NMR spectrum, two distinct [3]B species are identified. [3]B#1 is located at 17 ppm with a CQ of 2.6 MHz, while [3]B#2 is located at 13 ppm with a CQ of 2.6 MHz, often attributed to [3]B ring and [3]B non-ring species, respectively [60], [101], [103], [104], [105], [106]. However, as presented in Figure S8C, the isotropic projections of ^{11}B 3Q-MAS NMR maps for B15Nay glass series reveal that with the addition of Na in the glass network, the difference between the two [3]B species becomes less significant, rendering the distinction between the two [3]B species more challenging. This phenomenon has been also reported in previous paper by Du and Stebbins [107]. Lee and Lee [60] proposed that the [3]B#2 peak shifts to high frequency with increasing Na content. It explains the fit with a single peak located at 18.7 ppm with a CQ of 2.8 MHz for the 3QMAS ([3]B part) spectrum of CaNa-R2K1 glass. However, two [3]B species are still needed to reproduce the [3]B part of 1D ^{11}B MAS NMR spectrum (see Figure 4C). Therefore, in the context of polymerized glass compositions, the use of the ^{11}B 3Q-MAS NMR technique enables the separation of distinct [3]B species. However, its utility decreases notably when applied to depolymerized glass networks.

Secondly, the distinction between various [4]B species is accomplished through ^{11}B DQ-SQ NMR and Spin-Echo (SE) techniques. The SQ projection of a DQ-SQ NMR spectrum provides the information about species containing B-O-B bonds, enabling the distinction between [4]B species connected solely to other element sites and those linked to borate species

[108], [109], [110], [111], [112], [113]. The SE spectrum offers insights into the responses of different [4]B species to different echo times т (T_2 relaxation time effect) [106], thereby facilitating the separation between these various [4]B species. An illustrative example of the SQ projection of ^{11}B DQ-SQ NMR spectra, [11]B SE (with echo times of 75, 25, 0.05 ms from top to bottom), MAS-NMR spectra and their corresponding fits for the B15Na10 and CaNa-R2K1 glasses are presented in Figure S9. For the B15Na10 glass, the SQ projection reveals a single peak at -0.5 ppm corresponding to [4]B(3Si,1B) species [16], [106], [107]. The SE spectrum indicates at least two predominant [4]B species in the glass, one at -0.5 ppm (as observed in the SQ projection) and another at -2 ppm corresponding to [4]B(4Si,0B) species which cannot be observed in the SQ projection [16], [106], [107]. With increasing echo time, the relative intensity of the [4]B(3Si,1B) peak decreases, suggesting a shorter T_2 relaxation time for [4]B(3Si,1B) species compared to [4]B(4Si,0B) species. However, for the CaNa-R2K1 glass, both the SQ projection and SE spectrum exhibit a single peak at 0 ppm, indicating the presence of only one predominant species, namely [4]B(3Si,1B) in this glass. All fitting parameters for our investigated glasses are presented in Table. S6. The determined N_4 value will be used for the calculation of NBO content in next section and confront the obtained results with other spectroscopic methods.
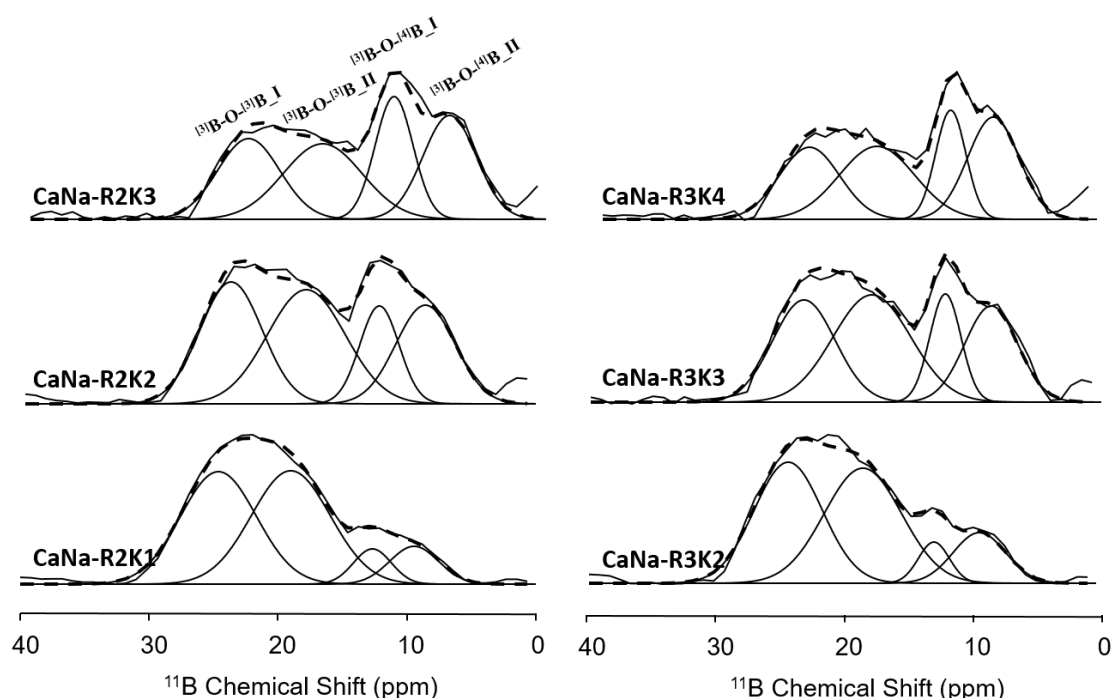

Figure 5. *DQ projection of ^{11}B DQ-SQ NMR maps of CaNa-RnKp glass series (dashed lines represent the decomposition spectra of [3]B-O-[3]B and [3]B-O-[4]B correlations using full Gaussian peaks (G/L = 1); two lines for reproducing [3]B-O-[3]B species and two lines for [3]B-O-[4]B species.*

Thirdly, as illustrated in Figure S9A, the DQ-SQ NMR map can provide information about correlations between borate species themselves, including [3]B-O-[3]B, [3]B-O-[4]B and [4]B-O-[4]B correlations. It is important to note that no significant amount of [4]B-O-[4]B connections was observed in our investigated glasses, according to DQ-SQ NMR maps. As presented in Figure S9B, the [3]B-O-[3]B and [3]B-O-[4]B correlations can be separated in DQ projection. Thus, we decomposed the DQ projections to determine the evolution of connectivity between borate species. The fit of DQ-SQ DQ projection of CaNa-RnKp glass series is presented in Figure 5. In general, the DQ projection is not quantitative for the determination of the correlation concentration because of the varying efficiency of Double-Quantum Coherence creation (DQC). This variation arises from the significant difference of CQ between [3]B (~2.6 MHz) and [4]B (~0.4 MHz) species, and from the differences in [n]B-O-[n]B distances ([4]B-O-[4]B > [3]B-O-[4]B > [3]B-O-[3]B) [108], [114]. However, two assumptions were made: first, due to the very short

recoupling time used in our DQ-SQ sequence (2 x 400 μs). According to some recent papers [109], [111], [115], a very short recoupling time allows for observing the spatial proximity regarding chemical connectivity. Second, assuming that the distribution of CQ or the distances of $[n]$B-O-$[n]$B bonds do not exhibit significant variations in similar glass systems, the DQC of each correlation remains relatively constant. Therefore, under the same experimental conditions, we may analyse the evolution of relative connectivity between borate species (justification see Section 4.2). The region with a more negative chemical shift corresponds to the $[3]$B-O-$[3]$B correlation region ($\delta = \delta[3]B + \delta[3]B$), while the other region corresponds to the $[3]$B-O-$[4]$B correlation region ($\delta = \delta[3]B + \delta[4]B$). To determine the apparent proportion of each correlation, we used two Gaussian peaks each for $[3]$B-O-$[3]$B and $[3]$B-O-$[4]$B correlations. The derived apparent $[3]$B-O-$[3]$B% for all investigated glasses is presented in Table 1 and it will be used for the comparison with Raman results in the following section.

4. Discussion

4.1 Degree of polymerization as observed by Raman, XPS and NMR spectroscopies

4.1.1 Comparison of apparent n value of Q^n units from Raman and indirectly calculated n value of Q^n units from NMR results

As previously mentioned, extensive research has attempted to use Raman spectroscopy to study the structural configuration of Q^n species in silicate glasses, with a general assignment of various Q^n peaks provided (see Figure 1). While the exact peak deconvolution in Raman spectra remains a subject of debate, the high-energy envelope (850-1250 cm^{-1}) can be used for quantitative determination of certain Q^n species in alkali and alkaline earth silicate glasses. This is evidenced by the fact that for a glass containing 40 mol. % Na_2O, the Q^n distribution obtained through three distinct independent techniques (^{29}Si NMR [33], Raman [19], and O 1s XPS [66]) is consistent within experimental errors. At the same time, Nesbitt et al. [19] and Moulton et al. [38] studied Na_2O-SiO_2 (NS) and BaO-SiO_2 (BaS) glass systems, respectively, and determined the Raman cross-section values for Q^2 (1.07 for NS and 0.85 for BaS) and Q^3 (0.97 for NS and 1.22 for BaS) species with the help of ^{29}Si NMR technique. However, it is worth mentioning that the glass systems in these studies are binary, with relatively simple silicate network structures. Consequently, the corresponding ^{29}Si NMR and ^{17}O 1s spectra can clearly distinguish between different Q^n peaks and between O 1s (NBO) and O 1s (BO), providing a reliable reference for Raman peak deconvolution and cross-section value determination is available. In more complex glass systems (i.e. ternary), such as Na_2O-Al_2O_3-SiO_2 [34] and CaO-Al_2O_3-B_2O_3-SiO_2 [106] systems, Raman and ^{29}Si NMR spectra have also been discussed in combination; however, the ^{29}Si NMR spectra in these cases become more challenging to interpret because of the lack of resolution. There has been no direct comparison between Raman and ^{29}Si NMR results in these studies.

Thus, in this study, the polymerization degree of the silicate network (average n value of Q^n units) was determined directly through the decomposition of Raman spectra and indirectly through Q^n calculation via ^{11}B and ^{27}Al NMR results by using Eq. 2 and 3 (see Table 1). Two assumptions were made for Eq. 2 and 3 in our investigated glasses. We assume that there is no B-NBO present and that the $[5]$Al and $[6]$Al species ($[5/6]$Al) would not significantly impact the NBO content, given that the content of Al_2O_3 (< 5 mol.%) and the total proportion of $[5/6]$Al species (< 10%) are relatively low. The comparison between Raman and NMR approaches is plotted in Figure 6. The plotted data reveals that the majority of data points are almost aligned around the same linear trend, indicating that these two methods are consistent for determining the Q^n distribution for most investigated aluminoborosilicate glass. We observe that increasing in n value of Q^n by NMR from 1.3 (CaNa-R2K1) to 4.0 (B15Na10) is positively correlated with the increase in n value by Raman from 2.7 (CaNa-R2K1) to 3.7 (B15Na10), indicating that the suggested peak assignment in Raman spectra is consistent. For glasses with extremely low

silica content (i.e. glasses with very low polymerization degrees glasses), such as CaNa-R2K1, Ca-R2K1, CaNa-R3K2 and Ca-R3K2 glasses, the data points deviate from the correlation line, and the derived n values from NMR are significantly lower (1.2–2.2) than those obtained from Raman spectra (2.7–2.8). This difference could arise from the calculation of NBO content via ^{11}B and ^{27}Al NMR spectra, which represents total NBO rather than solely silicon-coordinated NBO (Si-NBO). In the case of glasses with low polymerization degrees, a significant proportion of NBO is linked with boron species (B-NBO) according to the model of Dell [35], indistinguishable by ^{11}B and ^{27}Al NMR spectroscopy. Indeed, this limitation highlights a drawback of using calculation of NBO content based on ^{11}B and ^{27}Al NMR results for Q^n calculation among B-NBO contained glasses. Another hypothesis is that there is a change in the Raman cross section parameters for each Q^n species as function of glass composition involving non-linear Q^n change as previously mentioned in Na_2O-SiO_2 and BaO-SiO_2 glass systems. Finally, it should be pointed out that both methods have different ways of characterizing the same sample: the composition fluctuations from one point to another in a piece of glass, the Raman spectra which correspond to punctual analysis with a laser beam, can be significantly different; whereas for NMR, the spectra obtained correspond to the sum of all spin nuclei present in the rotor. This could have different implications depending on the glass composition and degree of polymerization. Therefore, all the raised points imply that investigating the glass degree of polymerization through quantitative Q^n analysis cannot be reasonably accomplished with a single method approach only and that several analytical tools have to be used.
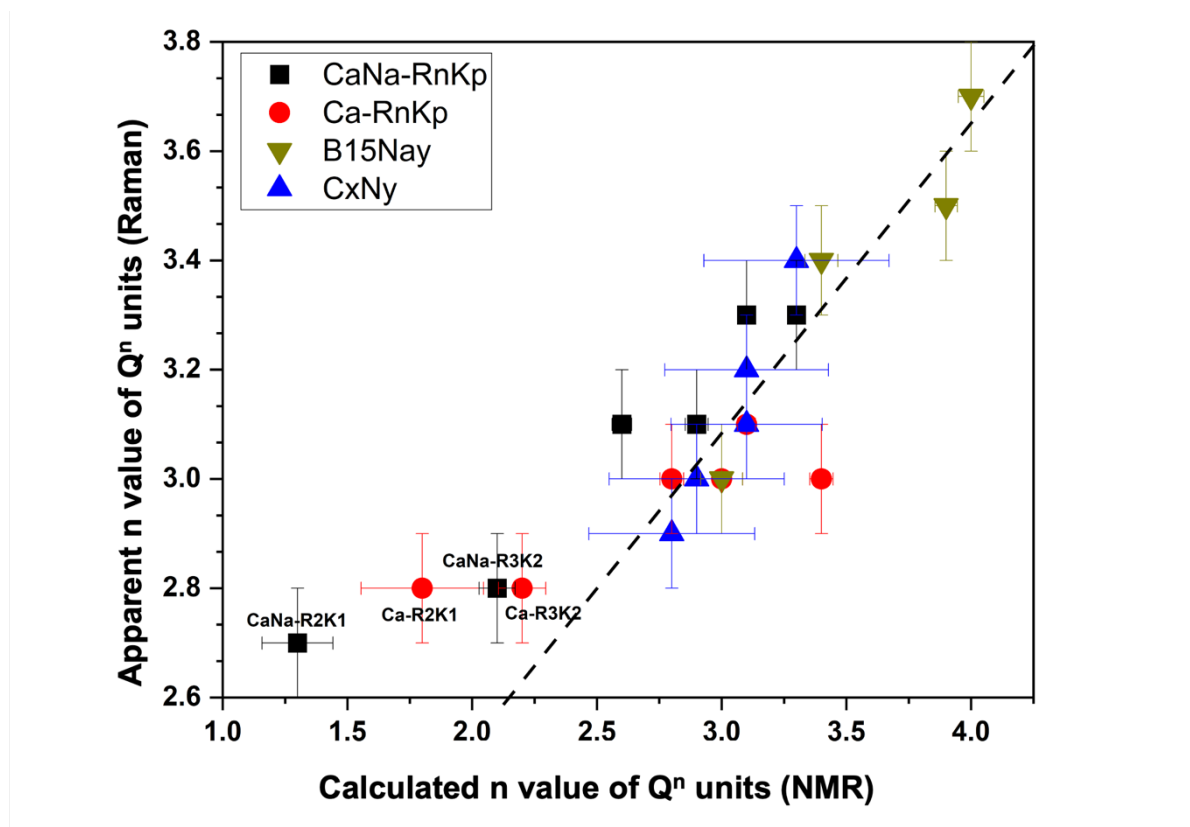

Figure 6. *Comparison of average (apparent) n value of Q^n units determined via NMR and Raman methods (dashed line represents the correlation line of this two methods). The error bars were determined from standard deviation calculation and also replicated measurements.*

4.1.2 Oxygen speciation from XPS and indirect NMR results

Another way of determining the degree of glass polymerization is to investigate the oxygen speciation. There is a good agreement in the NBO% of the binary K_2O-SiO_2 glasses when using ^{17}O NMR [116] and XPS (O1s) [117]. However, this approach is much more complicated

if direct oxygen species characterization is to be conducted (i.e. glass enrichment with ^{17}O isotopes for NMR). In the present work, we determined the O speciation directly through O 1s XPS spectra decomposition and indirectly through calculation via ^{11}B and ^{27}Al NMR results by using Eq. 3 (as shown in Table 1). The comparison of XPS and NMR results are presented in Figure 7. We reported the one to one dashed line considering that the determination of NBO% values is directly quantitative using O 1s XPS [118].
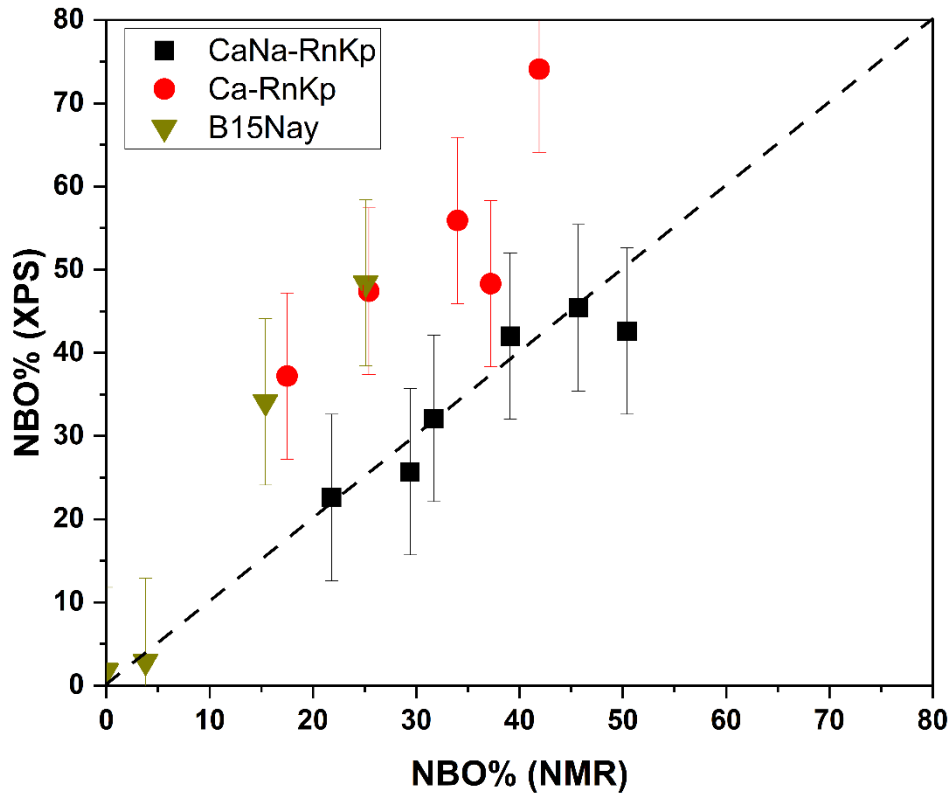
Figure 7. *Comparison of NBO content determined via NMR and XPS methods (dashed line represents the equality line). The NBO content from NMR has been determined indirectly with Eq. 3 and the obtained results on N_4 and Al speciation. The NBO content from XPS is obtained from the subsequent fitting as shown in Figure 2. Owing to the large uncertainty in the XPS fitting, the error bars on the NBO is large.*

The XPS and NMR results show relatively good agreement for the CaNa-RnKp series, slightly less so for the Ca-RnKp series, and even less for the B15Nay series. However, overall, the two sets of results are consistent with each other, supporting the validity of our peak decompositions of the XPS spectra in the NBO and BO regions. For Ca-RnKp series, the NBO(XPS)% values exceed those of NBO(NMR)%. This discrepancy could be due to two factors. The first one is the drawback inherent to the technique, given that XPS is a surface analysis technique, and it has been shown that the glass surface could have higher concentration of depolymerized network units as compared to the bulk glass itself [118], while the NMR analysis provide the bulk glass structure information. The second cause is also likely due to our incomplete knowledge of the O 1s XPS spectrum deconvolution. In fact, the literature data on that topic is limited and it would require more advanced investigations to have a more accurate view of the O 1s XPS spectrum deconvolution. It may arise from the presence of $^{[5]}Al$ and $^{[6]}Al$ species in this series, which complicates the interpretation of XPS spectra because no information regarding the oxygen environment connected to $^{[5]}Al$ and $^{[6]}Al$ species has been reported in XPS (O 1s) spectra. Hence, it is essential to highlight that determining the NBO content in low-polymerized aluminoborosilicate glasses containing only Ca using O 1s XPS spectra may necessitate complementary verification through alternative characterization methods.

Interestingly, Matsumoto et al. [23], in their study of alkali-silicate glasses across various systems (M_2O-SiO_2, M = Li, Na, K, Rb, Cs), mentioned that the O 1s binding energy can be used to evaluate the basicity of the glass. According to these authors, there is a strong linear relationship between binding energy (O 1s) and the glass optical basicity (Λ_{glass}). Recent work on iodine incorporation by Morizet el al. [119] also reported a negative linear correlation between O binding energy and calculated glass optical basicity. By extent, it suggests that at some point O speciation is related to the glass optical basicity that could constitute a good proxy of the degree of glass polymerization. Thus, in the accompanying manuscript on glass structure (Part II), we will consider the optical basicity to compare structural variations across different samples.

4.1.3 [n]B-O-[n]B connections as obtained by Raman and NMR methods

As mentioned previously, the DQ projection cannot be considered as a quantitative analysis tool. Assuming that the distribution of CQ or the distances of [n]B-O-[n]B bonds within the same borate species do not exhibit significant variations in glass structures, we suggest that, under identical experimental conditions, using the DQ projection to compare the relative concentration of [3]B-O-[3]B connections is feasible. As shown in Figure 8, a strong correlation between [3]B-O-[3]B% derived from DQ projections and N_4 value derived from ^{11}B NMR spectra is observed across the different glass systems studied in this work. We observed that a decrease in [3]B-O-[3]B% derived from [11]B DQ projection (from 80 to 50%) is correlated with an increase in N_4 value derived from ^{11}B NMR spectra (from 0.2 to 0.6). This negative correlation can also be derived from the literature data in which correction factors were used in order to realize the quantitative analysis of [n]B-O-[n]B correlation [108], as presented in Figure 8 (inset). This suggests a strong relationship between borate speciation and their correlations, indicating that our fit for DQ projection is reliable for exploring [n]B-O-[n]B connections under the same experimental conditions.

Another method for [n]B-O-[n]B connections analysis employed in this study is using the boron network region (1200–1600 cm^{-1}) in the Raman spectra. The results are presented in Table 1. The Raman-derived [3]B-O-[3]B% values show no significant variations, ranging from 50 to 60% for most of our investigated glasses. Only for B15Na20 and B15Na30 glasses, this value can reach 70%. This means the borate network does not have a preference for either [3]B-O-[3]B or [3]B-O-[4]B connections for a large range of glass compositions, which is not consistent with the results that we obtained by DQ-SQ NMR methods where [3]B-O-[3]B% values are strongly rely on the N_4 values. Consequently, the reliability of information regarding boron species connectivity in aluminoborosilicate glasses obtained from Raman spectra is currently questionable.
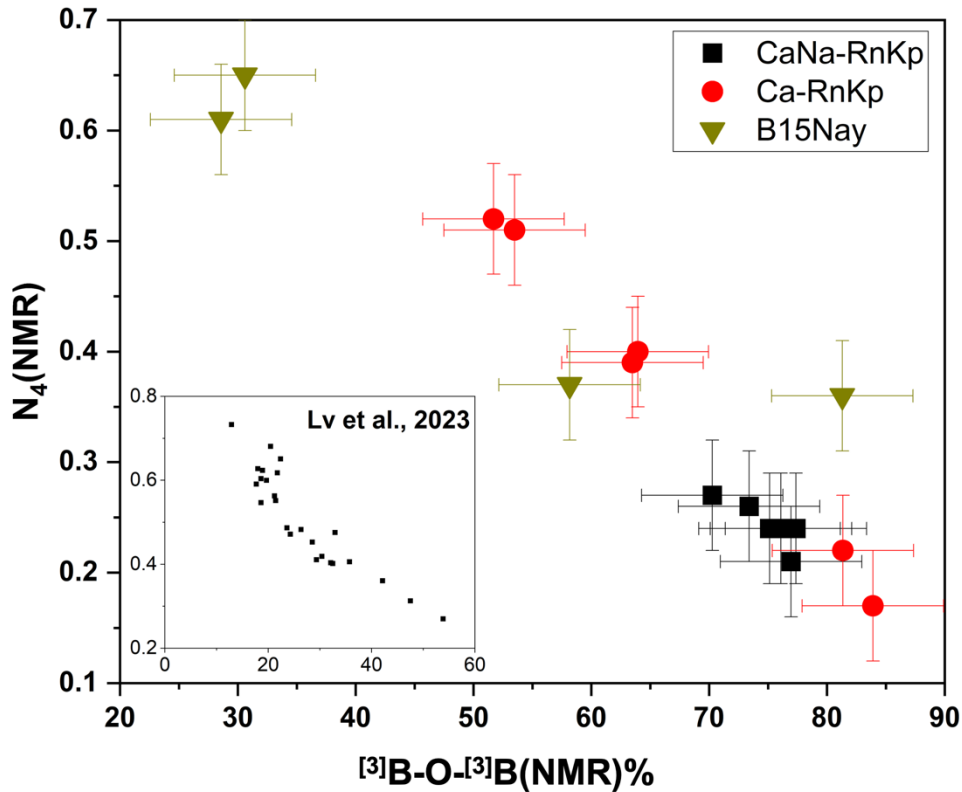
Figure 8. *Plots of [3]B-O-[3]B % values plotted against N_4 values of our investigated glasses as determined from NMR results: 1D [11]B spectrum fitting for N_4 and DQ-SQ DQ projection for [3]B-[3]B %. The inset contains data obtained from the literature (Lv et al., 2023 [108]), which shares the same axis units as the main figure.*

4.1.4 Ca and Na environment as observed by XAS and NMR methods

The discussion of environment of Ca and Na is focused on CaNa-RnKp glass series considering that only this glass series has both cations in its composition. The local environment of Ca was determined using K-edge EXAFS spectra shown in Figure 3, which provided information such as the average distance between Ca and the first nearest neighbour (average r_{Ca-O}) and the coordination number of Ca (CN_{Ca-O}). Meanwhile, the local environment of Na was assessed through ^{23}Na NMR spectra, where the chemical shift of [23]Na yielded comprehensive information on CN_{Na} and average r_{Na-O}. Both parameters exhibit a negative correlation with the chemical shift of [23]Na. Thus, we plotted the relation between average r_{Ca-O} and CN_{Ca-O} with δ_{Na} as presented in Figure 9A and 9B, respectively, for the glass series for which we have both the Ca K-edge EXAFS spectra and ^{23}Na MAS NMR spectra. We made the distinction between the CaNa-R2Kp and the CaNa-R3Kp glass series. The comparison shows a good correlation between the calcium and sodium environments in CaNa-RnKp glass series. When the isotropic chemical shift of Na increases from -0.5 to 6.5 ppm, the average r_{Ca-O} and CN_{Ca-O} decreases from 2.66 to 2.55 Å and from 6.4 to 5.8, respectively, indicating a potential relation between calcium and sodium local environments in glass. While the comparison of ^{23}Na NMR and Ca K-edge XAS results does not provide conclusive evidence for Ca-Na mixing, it is evident that, at least in glasses with high Ca and Na content, the overall chemical environment of non-network-forming cations changes synchronously rather than separately. Given that both Ca and Na ions are coordinated by oxygen, investigating the chemical environment of oxygen emerges as a promising avenue of research. This will be the focus of the subsequent manuscript on glass structure (Part II).
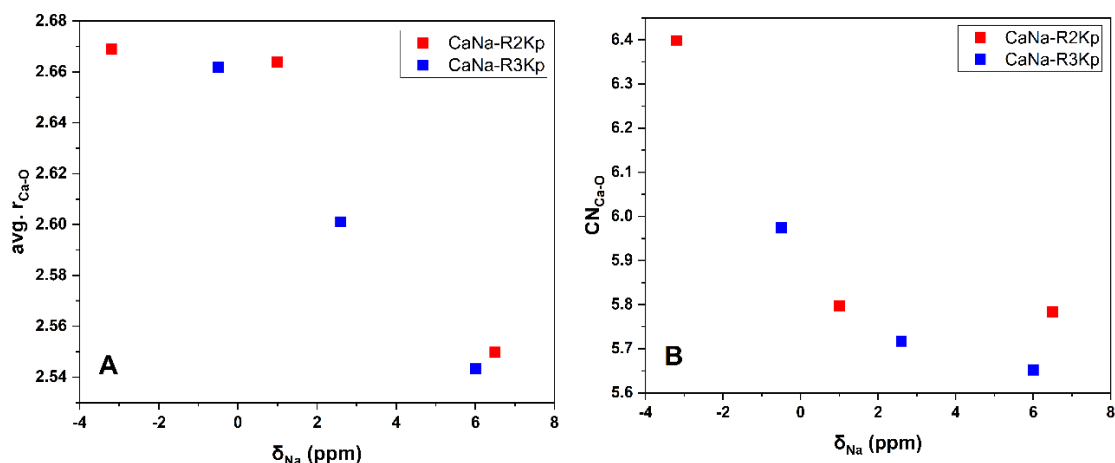
Figure 9. *Relationship between Na environment obtained by NMR spectroscopy and Ca environment obtained by XAS spectroscopy in the CaNa-RnKp glass series. The average distance of Ca-O (A) and the coordination number of Ca-O (B) against the chemical shift of ^{23}Na.*

5. Conclusions

In the present work, we used a combination of Raman, XPS, XAS and NMR techniques to investigate the structure of soda lime aluminoborosilicate glasses, including the polymerization degree of the silicate network (average *n* value of Q^n units), the content of non-bridging oxygen (NBO%), the connectivity between borate species ($^{[n]}B$-O-$^{[n]}B$%) and the chemical environment of Ca and Na cations. Firstly, our findings revealed that the decomposition of Raman spectra in the silicate network region allowed for the determination of the polymerization degree of the silicate network. The derived *n* values of Q^n units exhibited good agreement with those calculated from ^{11}B and ^{27}Al NMR spectra for glasses without B-NBO species. Furthermore, the decomposition of XPS O1s spectra enabled the determination of the NBO content, which also showed good consistency with the calculated values from ^{11}B and ^{27}Al NMR spectra. This approach addressed the need for incorporating ^{29}Si and ^{17}O NMR to analyse the Q^n distribution and NBO content, respectively. Secondly, the DQ projection of ^{11}B DQ-SQ NMR maps can be used to analyse the changes in relative connectivity between borate species across diverse glass compositions under uniform experimental conditions, while the decomposition of Raman spectra in the borate network region remains inconclusive. Thirdly, the Ca K-edge XAS spectra offer dependable insights into assessing the local environment of Ca, furnishing precise details regarding the first shell configuration that cannot be obtained through NMR analysis without ^{43}Ca enrichment. Also, we have presented a comprehensive analysis scheme for ^{11}B NMR spectra to distinguish boron species laying the groundwork for our future research endeavours.

This study underscores the insights provided by each structural probing technique and their combined advantages in robustly determining the Q^n distribution, NBO content and chemical environment of Ca and Na. It is important to note that our fitting process did not assume a priori the degree of polymerization. Therefore, this work is poised to mitigate contradictory reports on Q^n species and NBO content in the literature, facilitating a deeper understanding of the structure of silicate glasses.

Data availability statement

Data of presented results can be provided upon request.

Underlying and related material

Supplementary materials are available at https://doi.org/10.5281/zenodo.14266605.

Author contributions

Hanyu Hu: Investigation, Validation, Data curation, Writing – original draft preparation, review & editing.

Sami Soudani: Resources, Writing – review & editing.

Jonathan Hamon: Investigation, Writing – original draft preparation, review & editing.

Nicolas Trcera: Investigation, Writing – original draft preparation, review & editing.

Michael Paris: Supervision, Writing – review & editing.

Yann Morizet: Conceptualization, Methodology, Supervision, Resources, Writing – review & editing.

Competing interests

The authors declare that they have no competing interests.

Acknowledgement

References

[1] Januchta, K.; Youngman, R. E.; Goel, A.; Bauchy, M.; Rzoska, S. J.; Bockowski, M.; Smedskjaer, M. M. Structural Origin of High Crack Resistance in Sodium Aluminoborate Glasses. *Journal of Non-Crystalline Solids* 2017, *460*, 54–65. https://doi.org/10.1016/j.jnoncrysol.2017.01.019.

[2] Smedskjaer, M. M.; Zheng, Q.; Mauro, J. C.; Potuzak, M.; Mørup, S.; Yue, Y. Sodium Diffusion in Boroaluminosilicate Glasses. *Journal of Non-Crystalline Solids* 2011, *357* (22–23), 3744–3750. https://doi.org/10.1016/j.jnoncrysol.2011.07.008.

[3] Bødker, M. S.; Christensen, R.; Sørensen, L. G.; Østergaard, M. B.; Youngman, R. E.; Mauro, J. C.; Smedskjaer, M. M. Predicting Cation Interactions in Alkali Aluminoborate Glasses Using Statistical Mechanics. *Journal of Non-Crystalline Solids* 2020, *544*, 120099. https://doi.org/10.1016/j.jnoncrysol.2020.120099.

[4] Varshneya, A. K.; Mauro, J. C. Chapter 1 - Introduction. In *Fundamentals of Inorganic Glasses (Third Edition)*; Varshneya, A. K., Mauro, J. C., Eds.; Elsevier, 2019; pp 1–18. https://doi.org/10.1016/B978-0-12-816225-5.00001-8.

[5] Wallenberger, F. T.; Bingham, P. A. *Fiberglass and Glass Technology*; Springer US: Boston, MA, 2010. https://doi.org/10.1007/978-1-4419-0736-3.

[6] Fitzer, E.; Kleinholz, R.; Tiesler, H.; Stacey, M. H.; De Bruyne, R.; Lefever, I.; Heine, M. Fibers, 5. Synthetic Inorganic. In *Ullmann's Encyclopedia of Industrial Chemistry*; John Wiley & Sons, Ltd, 2000. https://doi.org/10.1002/14356007.a11_001.

[7] Lonergan, C.; George, J.; Cutforth, D.; Jin, T.; Cholsaipant, P.; Sannoh, S.; Skidmore, C.; Piepel, G.; Russell, R.; Vienna, J. Enhanced Hanford Low- Activity Waste Glass Property Data Development: Phase 3.

[8] Chick, L. A.; Piepel, G. F. Statistically Designed Optimization of a Glass Composition. *Journal of the American Ceramic Society* 1984, *67* (11), 763–768. https://doi.org/10.1111/j.1151-2916.1984.tb19514.x.

[9] Russell, R. L.; McCarthy, B. P.; Skidmore, C. H.; Lang, J. B.; Meline, J. M.; Sannoh, S. E.; Gervasio, V.; Stanfill, B. A.; Lonergan, C. E.; Cordova, E. A. Enhanced Hanford Low-Activity Waste Glass Property Data Development: Phase 2 - PNNL-28838 Rev 2, EWG-RPT-021 Rev. 2.

[10] Davis, M. C.; Kaseman, D. C.; Parvani, S. M.; Sanders, K. J.; Grandinetti, P. J.; Massiot, D.; Florian, P. $Q^{(n)}$ Species Distribution in $K_2O \cdot 2SiO_2$ Glass by ^{29}Si Magic Angle Flipping NMR. *J. Phys. Chem. A* 2010, *114* (17), 5503–5508. https://doi.org/10.1021/jp100530m.

[11] Henderson, G. S. THE STRUCTURE OF SILICATE MELTS: A GLASS PERSPECTIVE. *The Canadian Mineralogist* 2005, *43* (6), 1921–1958. https://doi.org/10.2113/gscanmin.43.6.1921.

[12] Poe, B. T.; McMillan, P. F.; Angell, C. A.; Sato, R. K. Al and Si Coordination in SiO_2-Al_2O_3 Glasses and Liquids: A Study by NMR and IR Spectroscopy and MD Simulations. *Chemical Geology* 1992, *96* (3), 333–349. https://doi.org/10.1016/0009-2541(92)90063-B.

[13] Zheng, Q. J.; Youngman, R. E.; Hogue, C. L.; Mauro, J. C.; Potuzak, M.; Smedskjaer, M. M.; Yue, Y. Z. Structure of Boroaluminosilicate Glasses: Impact of $[Al_2O_3]/[SiO_2]$ Ratio on the Structural Role of Sodium. *Phys. Rev. B* 2012, *86* (5), 054203. https://doi.org/10.1103/PhysRevB.86.054203.

[14] Jolivet, V.; Jossé, L.; Rivoal, M.; Paris, M.; Morizet, Y.; Carole, L.; Suzuki-Muresan, T. Quantification of Boron in Aluminoborosilicate Glasses Using Raman and ^{11}B NMR. *Journal of Non-Crystalline Solids* 2019, *511*, 50–61. https://doi.org/10.1016/j.jnoncrysol.2018.12.038.

[15] Du, L.-S.; Stebbins, J. F. Network Connectivity in Aluminoborosilicate Glasses: A High-Resolution ^{11}B, ^{27}Al and ^{17}O NMR Study. *Journal of Non-Crystalline Solids* 2005, *351* (43–45), 3508–3520. https://doi.org/10.1016/j.jnoncrysol.2005.08.033.

[16] Du, L.-S.; Stebbins, J. F. Solid-State NMR Study of Metastable Immiscibility in Alkali Borosilicate Glasses. *Journal of Non-Crystalline Solids* 2003, *315* (3), 239–255. https://doi.org/10.1016/S0022-3093(02)01604-6.

[17] Lee, S. K.; Kim, H.-I.; Kim, E. J.; Mun, K. Y.; Ryu, S. Extent of Disorder in Magnesium Aluminosilicate Glasses: Insights from [27] Al and [17] O NMR. *J. Phys. Chem. C* 2016, *120* (1), 737–749. https://doi.org/10.1021/acs.jpcc.5b10799.

[18] Bødker, M. S.; Youngman, R. E.; Mauro, J. C.; Smedskjaer, M. M. Mixed Alkali Effect in Silicate Glass Structure: Viewpoint of [29] Si Nuclear Magnetic Resonance and Statistical Mechanics. *J. Phys. Chem. B* 2020, *124* (45), 10292–10299. https://doi.org/10.1021/acs.jpcb.0c07980.

[19] Nesbitt, H. W.; Henderson, G. S.; Bancroft, G. M.; Neuville, D. R. Spectral Resolution and Raman Q^3 and Q^2 Cross Sections in ~40 Mol% Na_2O Glasses. *Chemical Geology* 2021, *562*, 120040. https://doi.org/10.1016/j.chemgeo.2020.120040.

[20] Manara, D.; Grandjean, A.; Neuville, D. R. Advances in Understanding the Structure of Borosilicate Glasses: A Raman Spectroscopy Study. *American Mineralogist* 2009, *94* (5–6), 777–784. https://doi.org/10.2138/am.2009.3027.

[21] Wang, P. W.; Zhang, L. Structural Role of Lead in Lead Silicate Glasses Derived from XPS Spectra. *Journal of Non-Crystalline Solids* 1996, *194* (1–2), 129–134. https://doi.org/10.1016/0022-3093(95)00471-8.

[22] Sprenger, D.; Bach, H.; Meisel, W.; Gütlich, P. XPS Study of Leached Glass Surfaces. *Journal of Non-Crystalline Solids* 1990, *126* (1–2), 111–129. https://doi.org/10.1016/0022-3093(90)91029-Q.

[23] Matsumoto, S.; Nanba, T.; Miura, Y. X-Ray Photoelectron Spectroscopy of Alkali Silicate Glasses. *Journal of the Ceramic Society of Japan* 1998, *106* (1232), 415–421. https://doi.org/10.2109/jcersj.106.415.

[24] Neuville, D. R.; Cormier, L.; Flank, A.-M.; Briois, V.; Massiot, D. Al Speciation and Ca Environment in Calcium Aluminosilicate Glasses and Crystals by Al and Ca K-Edge X-Ray Absorption Spectroscopy. *Chemical Geology* 2004, *213* (1–3), 153–163. https://doi.org/10.1016/j.chemgeo.2004.08.039.

[25] Le Cornec, D.; Cormier, L.; Galoisy, L.; Baptiste, B.; Trcera, N.; Izoret, L.; Calas, G. Molecular Structure of Amorphous Slags: An Experimental and Numerical Approach. *Journal of Non-Crystalline Solids* 2021, *556*, 120444. https://doi.org/10.1016/j.jnoncrysol.2020.120444.

[26] Cormier, L.; Cuello, G. J. Structural Investigation of Glasses along the $MgSiO_3$–$CaSiO_3$ Join: Diffraction Studies. *Geochimica et Cosmochimica Acta* 2013, *122*, 498–510. https://doi.org/10.1016/j.gca.2013.04.026.

[27] Cicconi, M. R.; Ligny, D. de; Gallo, T. M.; Neuville, D. R. Ca Neighbors from XANES Spectroscopy: A Tool to Investigate Structure, Redox, and Nucleation Processes in Silicate Glasses, Melts, and Crystals. *American Mineralogist* 2016, *101* (5), 1232–1235. https://doi.org/doi:10.2138/am-2016-5663.

[28] Morizet, Y.; Trcera, N.; Larre, C.; Rivoal, M.; Le Menn, E.; Vantelon, D.; Gaillard, F. X-Ray Absorption Spectroscopic Investigation of the Ca and Mg Environments in CO_2-Bearing Silicate Glasses. *Chemical Geology* 2019, *510*, 91–102. https://doi.org/10.1016/j.chemgeo.2019.02.014.

[29] Morizet, Y.; Trcera, N.; Suzuki-Muresan, T.; Soudani, S.; Fonda, E.; Paris, M. Local Environment of Iodine Dissolved as Iodate in High-Pressure Aluminoborosilicate Glasses: A I K-Edge x-Ray Absorption Spectroscopic Study. *J. Chem. Phys.* 2022, *156* (15), 154508. https://doi.org/10.1063/5.0089039.

[30] Stebbins, J. F.; Farnan, I.; Xue, X. The Structure and Dynamics of Alkali Silicate Liquids: A View from NMR Spectroscopy. *Chemical Geology* 1992, *96* (3–4), 371–385. https://doi.org/10.1016/0009-2541(92)90066-E.

[31] Larsen, F. H.; Farnan, I. [29]Si and ^{17}O (Q)CPMG-MAS Solid-State NMR Experiments as an Optimum Approach for Half-Integer Nuclei Having Long T_1 Relaxation Times. *Chemical Physics Letters* 2002, *357* (5–6), 403–408. https://doi.org/10.1016/S0009-2614(02)00520-1.

[32] Sun, K. FUNDAMENTAL CONDITION OF GLASS FORMATION*. *Journal of the American Ceramic Society* 1947, *30* (9), 277–281. https://doi.org/10.1111/j.1151-2916.1947.tb19654.x.

[33] Stebbins, J. F. Identification of Multiple Structural Species in Silicate Glasses by ^{29}Si NMR. *Nature* 1987, *330* (6147), 465–467. https://doi.org/10.1038/330465a0.

[34] Le Losq, C.; Neuville, D. R.; Florian, P.; Henderson, G. S.; Massiot, D. The Role of Al^{3+} on Rheology and Structural Changes in Sodium Silicate and Aluminosilicate Glasses and Melts. *Geochimica et Cosmochimica Acta* 2014, *126*, 495–517. https://doi.org/10.1016/j.gca.2013.11.010.

[35] Dell, W. J.; Bray, P. J.; Xiao, S. Z. ^{11}B NMR Studies and Structural Modeling of Na$_2$O-B$_2$O$_3$-SiO$_2$ Glasses of High Soda Content. *Journal of Non-crystalline Solids* 1983, *58*, 1–16. https://doi.org/10.1016/0022-3093(83)90097-2.

[36] Morizet, Y.; Vuilleumier, R.; Paris, M. A NMR and Molecular Dynamics Study of CO$_2$-Bearing Basaltic Melts and Glasses. *Chemical Geology* 2015, *418*, 89–103. https://doi.org/10.1016/j.chemgeo.2015.03.021.

[37] Morizet, Y.; Paris, M.; Gaillard, F.; Scaillet, B. Carbon Dioxide in Silica-Undersaturated Melt Part II: Effect of CO$_2$ on Quenched Glass Structure. *Geochimica et Cosmochimica Acta* 2014, *144*, 202–216. https://doi.org/10.1016/j.gca.2014.08.034.

[38] Moulton, B. J. A.; Silva, L. D.; Doerenkamp, C.; Lozano, H.; Zanotto, E. D.; Eckert, H.; Pizani, P. S. Speciation and Polymerization in a Barium Silicate Glass: Evidence from ^{29}Si NMR and Raman Spectroscopies. *Chemical Geology* 2021, *586*, 120611. https://doi.org/10.1016/j.chemgeo.2021.120611.

[39] Maekawa, H.; Nakao, T.; Shimokawa, S.; Yokokawa, T. Coordination of Sodium Ions in NaAlO$_2$-SiO$_2$ Melts: A High Temperature ^{23}Na NMR Study. *Physics and Chemistry of Minerals* 1997, *24* (1), 53–65. https://doi.org/10.1007/s002690050017.

[40] Edén, M.; Sundberg, P.; Stålhandske, C. The Split Network Analysis for Exploring Composition–Structure Correlations in Multi-Component Glasses: II. Multinuclear NMR Studies of Alumino-Borosilicates and Glass-Wool Fibers. *Journal of Non-Crystalline Solids* 2011, *357* (6), 1587–1594. https://doi.org/10.1016/j.jnoncrysol.2010.11.101.

[41] Charpentier, T.; Menziani, M. C.; Pedone, A. Computational Simulations of Solid State NMR Spectra: A New Era in Structure Determination of Oxide Glasses. *RSC Adv.* 2013, *3* (27), 10550. https://doi.org/10.1039/c3ra40627j.

[42] Hung, I.; Gan, Z.; Gor'kov, P. L.; Kaseman, D. C.; Sen, S.; LaComb, M.; Stebbins, J. F. Detection of "Free" Oxide Ions in Low-Silica Ca/Mg Silicate Glasses: Results from ^{17}O →^{29}Si HETCOR NMR. *Journal of Non-Crystalline Solids* 2016, *445–446*, 1–6. https://doi.org/10.1016/j.jnoncrysol.2016.04.042.

[43] Stebbins, J. F. Anionic Speciation in Sodium and Potassium Silicate Glasses near the Metasilicate ([Na,K]$_2$SiO$_3$) Composition: ^{29}Si, ^{17}O, and ^{23}Na MAS NMR. *Journal of Non-Crystalline Solids: X* 2020, *6*, 100049. https://doi.org/10.1016/j.nocx.2020.100049.

[44] Ackerson, M. R.; Cody, G. D.; Mysen, B. O. ^{29}Si Solid State NMR and Ti K-Edge XAFS Pre-Edge Spectroscopy Reveal Complex Behavior of Ti in Silicate Melts. *Prog Earth Planet Sci* 2020, *7* (1), 14. https://doi.org/10.1186/s40645-020-00326-2.

[45] Matson, D. W.; Sharma, S. K.; Philpotts, J. A. The Structure of High-Silica Alkali-Silicate Glasses. A Raman Spectroscopic Investigation. *Journal of Non-Crystalline Solids* 1983, *58* (2–3), 323–352. https://doi.org/10.1016/0022-3093(83)90032-7.

[46] Zakaznova-Herzog, V. P.; Malfait, W. J.; Herzog, F.; Halter, W. E. Quantitative Raman Spectroscopy: Principles and Application to Potassium Silicate Glasses. *Journal of Non-Crystalline Solids* 2007, *353* (44–46), 4015–4028. https://doi.org/10.1016/j.jnoncrysol.2007.06.033.

[47] Neuville, D. R.; De Ligny, D.; Henderson, G. S. Advances in Raman Spectroscopy Applied to Earth and Material Sciences. *Reviews in Mineralogy and Geochemistry* 2014, *78* (1), 509–541. https://doi.org/10.2138/rmg.2013.78.13.

[48] Frantz, J. D.; Mysen, B. O. Raman Spectra and Structure of BaO-SiO$_2$ SrO-SiO$_2$ and CaO-SiO$_2$ Melts to 1600°C. *Chemical Geology* 1995, *121* (1–4), 155–176. https://doi.org/10.1016/0009-2541(94)00127-T.

[49] McMillan, P. Structural Studies of Silicate Glasses and Melts-Applications and Limitations of Raman Spectroscopy. *American Mineralogist* 1984, *69* (7–8), 622–644.

[50] Angeli, F.; Villain, O.; Schuller, S.; Charpentier, T.; De Ligny, D.; Bressel, L.; Wondraczek, L. Effect of Temperature and Thermal History on Borosilicate Glass

Structure. *Phys. Rev. B* 2012, *85* (5), 054110. https://doi.org/10.1103/PhysRevB.85.054110.

[51] Mysen, B. O.; Virgo, D.; Scarfe, C. M. Relations between the Anionic Structure and Viscosity of Silicate Melts-a Raman Spectroscopic Study. *American Mineralogist* 1980, *65* (7–8), 690–710.

[52] Mysen, B. O.; Virgo, D.; Seifert, F. A. The Structure of Silicate Melts: Implications for Chemical and Physical Properties of Natural Magma. *Reviews of Geophysics* 1982, *20* (3), 353–383. https://doi.org/10.1029/RG020i003p00353.

[53] Park, S. Y.; Lee, S. K. Structure and Disorder in Basaltic Glasses and Melts: Insights from High-Resolution Solid-State NMR Study of Glasses in Diopside–Ca-Tschermakite Join and Diopside–Anorthite Eutectic Composition. *Geochimica et Cosmochimica Acta* 2012, *80*, 125–142. https://doi.org/10.1016/j.gca.2011.12.002.

[54] Aguiar, P. M.; Michaelis, V. K.; McKinley, C. M.; Kroeker, S. Network Connectivity in Cesium Borosilicate Glasses: ^{17}O Multiple-Quantum MAS and Double-Resonance NMR. *Journal of Non-Crystalline Solids* 2013, *363*, 50–56. https://doi.org/10.1016/j.jnoncrysol.2012.12.010.

[55] Angeli, F.; Charpentier, T.; Gin, S.; Petit, J. C. ^{17}O 3Q-MAS NMR Characterization of a Sodium Aluminoborosilicate Glass and Its Alteration Gel. *Chemical Physics Letters* 2001, *341* (1–2), 23–28. https://doi.org/10.1016/S0009-2614(01)00423-7.

[56] Angeli, F.; Charpentier, T.; Gaillard, M.; Jollivet, P. Influence of Zirconium on the Structure of Pristine and Leached Soda-Lime Borosilicate Glasses: Towards a Quantitative Approach by ^{17}O MQMAS NMR. *Journal of Non-Crystalline Solids* 2008, *354* (31), 3713–3722. https://doi.org/10.1016/j.jnoncrysol.2008.03.046.

[57] Angeli, F.; Charpentier, T.; Molières, E.; Soleilhavoup, A.; Jollivet, P.; Gin, S. Influence of Lanthanum on Borosilicate Glass Structure: A Multinuclear MAS and MQMAS NMR Investigation. *Journal of Non-Crystalline Solids* 2013, *376*, 189–198. https://doi.org/10.1016/j.jnoncrysol.2013.05.042.

[58] Bisbrouck, N.; Bertani, M.; Angeli, F.; Charpentier, T.; Ligny, D.; Delaye, J.; Gin, S.; Micoulaut, M. Impact of Magnesium on the Structure of Aluminoborosilicate Glasses: A Solid-state NMR and Raman Spectroscopy Study. *J Am Ceram Soc* 2021, *104* (9), 4518–4536. https://doi.org/10.1111/jace.17876.

[59] Du, L.-S.; Stebbins, J. F. Site Connectivities in Sodium Aluminoborate Glasses: Multinuclear and Multiple Quantum NMR Results. *Solid State Nuclear Magnetic Resonance* 2005, *27* (1–2), 37–49. https://doi.org/10.1016/j.ssnmr.2004.08.003.

[60] Lee, A. C.; Lee, S. K. Effect of Composition on Structural Evolution and NMR Parameters of Quadrupolar Nuclides in Sodium Borate and Aluminoborosilicate Glasses: A View from High-Resolution ^{11}B, ^{27}Al, and ^{17}O Solid-State NMR. *Journal of Non-Crystalline Solids* 2021, *555*, 120271. https://doi.org/10.1016/j.jnoncrysol.2020.120271.

[61] Lee, S. K.; Lee, B. H. Atomistic Origin of Germanate Anomaly in GeO_2 and Na-Germanate Glasses: Insights from Two-Dimensional ^{17}O NMR and Quantum Chemical Calculations. *J. Phys. Chem. B* 2006, *110* (33), 16408–16412. https://doi.org/10.1021/jp063847b.

[62] Lee, S. K.; Stebbins, J. F. The Distribution of Sodium Ions in Aluminosilicate Glasses: A High-Field Na-23 MAS and 3Q MAS NMR Study. *Geochimica et Cosmochimica Acta* 2003, *67* (9), 1699–1709. https://doi.org/10.1016/S0016-7037(03)00026-7.

[63] Lee, S. K.; Stebbins, J. F. Effects of the Degree of Polymerization on the Structure of Sodium Silicate and Aluminosilicate Glasses and Melts: An ^{17}O NMR Study. *Geochimica et Cosmochimica Acta* 2009, *73* (4), 1109–1119. https://doi.org/10.1016/j.gca.2008.10.040.

[64] Lee, S. K.; Sung, S. The Effect of Network-Modifying Cations on the Structure and Disorder in Peralkaline Ca–Na Aluminosilicate Glasses: O-17 3QMAS NMR Study. *Chemical Geology* 2008, *256* (3–4), 326–333. https://doi.org/10.1016/j.chemgeo.2008.07.019.

[65] Nesbitt, H. W.; Henderson, G. S.; Bancroft, G. M.; O'Shaughnessy, C. Electron Densities over Si and O Atoms of Tetrahedra and Their Impact on Raman Stretching Frequencies

and Si-NBO Force Constants. *Chemical Geology* 2017, *461*, 65–74. https://doi.org/10.1016/j.chemgeo.2016.11.022.

[66] Nesbitt, H. W.; Bancroft, G. M.; Henderson, G. S.; Ho, R.; Dalby, K. N.; Huang, Y.; Yan, Z. Bridging, Non-Bridging and Free (O^{2-}) Oxygen in Na_2O-SiO_2 Glasses: An X-Ray Photoelectron Spectroscopic (XPS) and Nuclear Magnetic Resonance (NMR) Study. *Journal of Non-Crystalline Solids* 2011, *357* (1), 170–180. https://doi.org/10.1016/j.jnoncrysol.2010.09.031.

[67] Morizet, Y.; Soudani, S.; Hamon, J.; Paris, M.; La, C.; Gautron, E. Iodine Dissolution Mechanisms in High-Pressure Aluminoborosilicate Glasses and Their Relationship to Oxygen Speciation. *J. Mater. Chem. A* 2023, *11* (42), 22891–22905. https://doi.org/10.1039/D3TA05344J.

[68] Neuville, D. R.; Cormier, L.; Massiot, D. Al Environment in Tectosilicate and Peraluminous Glasses: A ^{27}Al MQ-MAS NMR, Raman, and XANES Investigation. *Geochimica et Cosmochimica Acta* 2004, *68* (24), 5071–5079. https://doi.org/10.1016/j.gca.2004.05.048.

[69] Soudani, S.; Paris, M.; Morizet, Y. Influence of High-Pressure on the Short-Range Structure of Ca or Na Aluminoborosilicate Glasses from ^{11}B and ^{27}Al Solid-State NMR. *Journal of Non-Crystalline Solids* 2024, *638*, 123085. https://doi.org/10.1016/j.jnoncrysol.2024.123085.

[70] Morizet, Y.; Hamon, J.; La, C.; Jolivet, V.; Suzuki-Muresan, T.; Paris, M. Immobilization of ^{129}I in Nuclear Waste Glass Matrixes Synthesized under High-Pressure Conditions: An Experimental Study. *J. Mater. Chem. A* 2021, *9* (42), 23902–23915. https://doi.org/10.1039/D1TA05011G.

[71] Fairley, N.; Fernandez, V.; Richard-Plouet, M.; Guillot-Deudon, C.; Walton, J.; Smith, E.; Flahaut, D.; Greiner, M.; Biesinger, M.; Tougaard, S.; Morgan, D.; Baltrusaitis, J. Systematic and Collaborative Approach to Problem Solving Using X-Ray Photoelectron Spectroscopy. *Applied Surface Science Advances* 2021, *5*, 100112. https://doi.org/10.1016/j.apsadv.2021.100112.

[72] Flank, A.-M.; Cauchon, G.; Lagarde, P.; Bac, S.; Janousch, M.; Wetter, R.; Dubuisson, J.-M.; Idir, M.; Langlois, F.; Moreno, T.; Vantelon, D. LUCIA, a Microfocus Soft XAS Beamline. *Nuclear Instruments and Methods in Physics Research Section B: Beam Interactions with Materials and Atoms* 2006, *246* (1), 269–274. https://doi.org/10.1016/j.nimb.2005.12.007.

[73] Vantelon, D.; Trcera, N.; Roy, D.; Moreno, T.; Mailly, D.; Guilet, S.; Metchalkov, E.; Delmotte, F.; Lassalle, B.; Lagarde, P.; Flank, A.-M. The LUCIA Beamline at SOLEIL. *J Synchrotron Rad* 2016, *23* (2), 635–640. https://doi.org/10.1107/S1600577516000746.

[74] Ravel, B.; Newville, M. *ATHENA* , *ARTEMIS* , *HEPHAESTUS* : Data Analysis for X-Ray Absorption Spectroscopy Using *IFEFFIT*. *J Synchrotron Rad* 2005, *12* (4), 537–541. https://doi.org/10.1107/S0909049505012719.

[75] Project, T. M. Materials Data on CaO by Materials Project. 2020. https://doi.org/10.17188/1201098.

[76] Project, T. M. Materials Data on $CaAl_2(SiO_4)_2$ by Materials Project. 2019. https://doi.org/10.17188/1711288.

[77] Eckersley, M. C.; Gaskell, P. H.; Barnes, A. C.; Chieux, P. The Environment of Ca Ions in Silicate Glasses. *Journal of Non-Crystalline Solids* 1988, *106* (1–3), 132–136. https://doi.org/10.1016/0022-3093(88)90246-3.

[78] Cormier, L.; Calas, G.; Gaskell, P. H. Cationic Environment in Silicate Glasses Studied by Neutron Diffraction with Isotopic Substitution. *Chemical Geology* 2001, *174* (1–3), 349–363. https://doi.org/10.1016/S0009-2541(00)00325-9.

[79] Hahn, E. L. Spin Echoes. *Phys. Rev.* 1950, *80* (4), 580–594. https://doi.org/10.1103/PhysRev.80.580.

[80] Kentgens, A. P. M.; Verhagen, R. Advantages of Double Frequency Sweeps in Static, MAS and MQMAS NMR of Spin I = 3/2 Nuclei. *Chemical Physics Letters* 1999, *300* (3), 435–443. https://doi.org/10.1016/S0009-2614(98)01402-X.

[81] Edén, M.; Zhou, D.; Yu, J. Improved Double-Quantum NMR Correlation Spectroscopy of Dipolar-Coupled Quadrupolar Spins. *Chemical Physics Letters* 2006, *431* (4–6), 397–403. https://doi.org/10.1016/j.cplett.2006.09.081.

[82] Wang, Q.; Hu, B.; Lafon, O.; Trébosc, J.; Deng, F.; Amoureux, J. P. Double-Quantum Homonuclear NMR Correlation Spectroscopy of Quadrupolar Nuclei Subjected to Magic-Angle Spinning and High Magnetic Field. *Journal of Magnetic Resonance* 2009, *200* (2), 251–260. https://doi.org/10.1016/j.jmr.2009.07.009.

[83] Moulton, B. J. A.; Picinin, A.; Silva, L. D.; Doerenkamp, C.; Lozano, H.; Sampaio, D.; Zanotto, E. D.; Du, J.; Eckert, H.; Pizani, P. S. A Critical Evaluation of Barium Silicate Glass Network Polymerization. *Journal of Non-Crystalline Solids* 2022, *583*, 121477. https://doi.org/10.1016/j.jnoncrysol.2022.121477.

[84] Tricot, G. The Structure of Pyrex® Glass Investigated by Correlation NMR Spectroscopy. *Phys. Chem. Chem. Phys.* 2016, *18* (38), 26764–26770. https://doi.org/10.1039/C6CP02996E.

[85] Gervais, C.; Laurencin, D.; Wong, A.; Pourpoint, F.; Labram, J.; Woodward, B.; Howes, A. P.; Pike, K. J.; Dupree, R.; Mauri, F.; Bonhomme, C.; Smith, M. E. New Perspectives on Calcium Environments in Inorganic Materials Containing Calcium–Oxygen Bonds: A Combined Computational–Experimental ^{43}Ca NMR Approach. *Chemical Physics Letters* 2008, *464* (1–3), 42–48. https://doi.org/10.1016/j.cplett.2008.09.004.

[86] Cormier, L.; Neuville, D. R. Ca and Na Environments in Na_2O–CaO–Al_2O_3–SiO_2 Glasses: Influence of Cation Mixing and Cation-Network Interactions. *Chemical Geology* 2004, *213* (1–3), 103–113. https://doi.org/10.1016/j.chemgeo.2004.08.049.

[87] Lee, S. K.; Stebbins, J. F. Nature of Cation Mixing and Ordering in Na-Ca Silicate Glasses and Melts. *J. Phys. Chem. B* 2003, *107* (14), 3141–3148. https://doi.org/10.1021/jp027489y.

[88] Roselieb, K.; Jambon, A. Tracer Diffusion of Mg, Ca, Sr, and Ba in Na-Aluminosilicate Melts. *Geochimica et Cosmochimica Acta* 2002, *66* (1), 109–123. https://doi.org/10.1016/S0016-7037(01)00754-2.

[89] Cormier, L.; Ghaleb, D.; Neuville, D. R.; Delaye, J.-M.; Calas, G. Chemical Dependence of Network Topology of Calcium Aluminosilicate Glasses: A Computer Simulation Study. *Journal of Non-Crystalline Solids* 2003, *332* (1–3), 255–270. https://doi.org/10.1016/j.jnoncrysol.2003.09.012.

[90] Massiot, D.; Fayon, F.; Capron, M.; King, I.; Le Calvé, S.; Alonso, B.; Durand, J.-O.; Bujoli, B.; Gan, Z.; Hoatson, G. Modelling One- and Two-Dimensional Solid-State NMR Spectra: Modelling 1D and 2D Solid-State NMR Spectra. *Magn. Reson. Chem.* 2002, *40* (1), 70–76. https://doi.org/10.1002/mrc.984.

[91] Angeli, F.; Villain, O.; Schuller, S.; Ispas, S.; Charpentier, T. Insight into Sodium Silicate Glass Structural Organization by Multinuclear NMR Combined with First-Principles Calculations. *Geochimica et Cosmochimica Acta* 2011, *75* (9), 2453–2469. https://doi.org/10.1016/j.gca.2011.02.003.

[92] Xue, X.; Stebbins, J. F. ^{23}Na NMR Chemical Shifts and Local Na Coordination Environments in Silicate Crystals, Melts and Glasses. *Physics and Chemistry of Minerals* 1993, *20*, 297–307. https://doi.org/10.1007/BF00215100.

[93] Stebbins, J. Cation Sites in Mixed-Alkali Oxide Glasses: Correlations of NMR Chemical Shift Data with Site Size and Bond Distance. *Solid State Ionics* 1998, *112* (1–2), 137–141. https://doi.org/10.1016/S0167-2738(98)00224-0.

[94] Edén, M. Chapter Four - Update on ^{27}Al NMR Studies of Aluminosilicate Glasses. In *Annual Reports on NMR Spectroscopy*; Elsevier, 2020; Vol. 101, pp 285–410. https://doi.org/10.1016/bs.arnmr.2020.07.002.

[95] Kelsey, K. E.; Stebbins, J. F.; Singer, D. M.; Brown, G. E.; Mosenfelder, J. L.; Asimow, P. D. Cation Field Strength Effects on High Pressure Aluminosilicate Glass Structure: Multinuclear NMR and La XAFS Results. *Geochimica et Cosmochimica Acta* 2009, *73* (13), 3914–3933. https://doi.org/10.1016/j.gca.2009.03.040.

[96] Toplis, M. J.; Kohn, S. C.; Smith, M. E.; Poplett, I. J. F. Letter. Fivefold-Coordinated Aluminum in Tectosilicate Glasses Observed by Triple Quantum MAS NMR. *American Mineralogist* 2000, *85* (10), 1556–1560. https://doi.org/10.2138/am-2000-1031.

[97] Neuville, D. R.; Cormier, L.; Massiot, D. Al Coordination and Speciation in Calcium Aluminosilicate Glasses: Effects of Composition Determined by ^{27}Al MQ-MAS NMR and Raman Spectroscopy. *Chemical Geology* 2006, *229* (1), 173–185. https://doi.org/10.1016/j.chemgeo.2006.01.019.

[98] Neuville, D. R.; Cormier, L.; Montouillout, V.; Massiot, D. Local Al Site Distribution in Aluminosilicate Glasses by ^{27}Al MQMAS NMR. *Journal of Non-Crystalline Solids* 2007, *353* (2), 180–184. https://doi.org/10.1016/j.jnoncrysol.2006.09.035.

[99] Allwardt, J. R.; Stebbins, J. F.; Terasaki, H.; Du, L.-S.; Frost, D. J.; Withers, A. C.; Hirschmann, M. M.; Suzuki, A.; Ohtani, E. Effect of Structural Transitions on Properties of High-Pressure Silicate Melts: ^{27}Al NMR, Glass Densities, and Melt Viscosities. *American Mineralogist* 2007, *92* (7), 1093–1104. https://doi.org/10.2138/am.2007.2530.

[100] Angeli, F.; Delaye, J.; Charpentier, T.; Petit, J.-C.; Ghaleb, D.; Faucon, P. Investigation of Al–O–Si Bond Angle in Glass by ^{27}Al 3Q-MAS NMR and Molecular Dynamics. *Chemical Physics Letters* 2000, *320* (5), 681–687. https://doi.org/10.1016/S0009-2614(00)00277-3.

[101] Quintas, A.; Charpentier, T.; Majérus, O.; Caurant, D.; Dussossoy, J.-L.; Vermaut, P. NMR Study of a Rare-Earth Aluminoborosilicate Glass with Varying CaO-to-Na_2O Ratio. *Appl Magn Reson* 2007, *32* (4), 613–634. https://doi.org/10.1007/s00723-007-0041-0.

[102] Wu, J.; Stebbins, J. F. Effects of Cation Field Strength on the Structure of Aluminoborosilicate Glasses: High-Resolution ^{11}B, ^{27}Al and ^{23}Na MAS NMR. *Journal of Non-Crystalline Solids* 2009, *355* (9), 556–562. https://doi.org/10.1016/j.jnoncrysol.2009.01.025.

[103] Lee, S. K.; Mibe, K.; Fei, Y.; Cody, G. D.; Mysen, B. O. Structure of B_2O_3 Glass at High Pressure: A ^{11}B Solid-State NMR Study. *Phys. Rev. Lett.* 2005, *94* (16), 165507. https://doi.org/10.1103/PhysRevLett.94.165507.

[104] Montouillout, V.; Fan, H.; Del Campo, L.; Ory, S.; Rakhmatullin, A.; Fayon, F.; Malki, M. Ionic Conductivity of Lithium Borate Glasses and Local Structure Probed by High Resolution Solid-Sate NMR. *Journal of Non-Crystalline Solids* 2018, *484*, 57–64. https://doi.org/10.1016/j.jnoncrysol.2018.01.020.

[105] Lee, S. K.; Stebbins, J. F. Extent of Intermixing among Framework Units in Silicate Glasses and Melts. *Geochimica et Cosmochimica Acta* 2002, *66* (2), 303–309. https://doi.org/10.1016/S0016-7037(01)00775-X.

[106] Angeli, F.; Charpentier, T.; De Ligny, D.; Cailleteau, C. Boron Speciation in Soda-Lime Borosilicate Glasses Containing Zirconium: Boron Speciation in Soda-Lime Borosilicate Glasses. *Journal of the American Ceramic Society* 2010, *93* (9), 2693–2704. https://doi.org/10.1111/j.1551-2916.2010.03771.x.

[107] Du, L.-S.; Stebbins, J. F. Nature of Silicon−Boron Mixing in Sodium Borosilicate Glasses: A High-Resolution ^{11}B and ^{17}O NMR Study. *J. Phys. Chem. B* 2003, *107* (37), 10063–10076. https://doi.org/10.1021/jp034048l.

[108] Lv, P.; Stevensson, B.; Yu, Y.; Wang, T.; Edén, M. BO_3/BO_4 Intermixing in Borosilicate Glass Networks Probed by Double-Quantum ^{11}B NMR: What Factors Govern BO_4-BO_4 Formation? *J. Phys. Chem. C* 2023, *127* (40), 20026–20040. https://doi.org/10.1021/acs.jpcc.3c03577.

[109] Doumert, B.; Lecomte, F.; Tricot, G. Advanced Solid State 1D/2D NMR Investigation of the B_2O_3-$Zn(PO_3)_2$ Glasses. *Journal of Non-Crystalline Solids* 2020, *548*, 120325. https://doi.org/10.1016/j.jnoncrysol.2020.120325.

[110] Tricot, G.; Ben Tayeb, K.; Koudelka, L.; Mosner, P.; Vezin, H. Insertion of MoO_3 in Borophosphate Glasses Investigated by Magnetic Resonance Spectroscopies. *J. Phys. Chem. C* 2016, *120* (17), 9443–9452. https://doi.org/10.1021/acs.jpcc.6b02502.

[111] Tricot, G.; Saitoh, A.; Takebe, H. Intermediate Length Scale Organisation in Tin Borophosphate Glasses: New Insights from High Field Correlation NMR. *Phys. Chem. Chem. Phys.* 2015, *17* (44), 29531–29540. https://doi.org/10.1039/C5CP02095F.

[112] Muñoz-Senovilla, L.; Tricot, G.; Muñoz, F. Kinetic Fragility and Structure of Lithium Borophosphate Glasses Analysed by 1D/2D NMR. *Phys. Chem. Chem. Phys.* 2017, *19* (34), 22777–22784. https://doi.org/10.1039/C7CP04171C.

[113] Lee, S. K.; Lee, A. C.; Kweon, J. J. Probing Medium-Range Order in Oxide Glasses at High Pressure. *J. Phys. Chem. Lett.* 2021, *12* (4), 1330–1338. https://doi.org/10.1021/acs.jpclett.1c00055.

[114] Yu, Y.; Stevensson, B.; Edén, M. Direct Experimental Evidence for Abundant BO_4–BO_4 Motifs in Borosilicate Glasses From Double-Quantum ^{11}B NMR Spectroscopy. *J. Phys. Chem. Lett.* 2018, *9* (21), 6372–6376. https://doi.org/10.1021/acs.jpclett.8b02907.

[115] Tricot, G.; Raguenet, B.; Silly, G.; Ribes, M.; Pradel, A.; Eckert, H. P–O–B[3] Linkages in Borophosphate Glasses Evidenced by High Field ^{11}B/^{31}P Correlation NMR. *Chem. Commun.* 2015, *51* (45), 9284–9286. https://doi.org/10.1039/C5CC01992C.

[116] Stebbins, J. F.; Sen, S. Oxide Ion Speciation in Potassium Silicate Glasses: New Limits from 17O NMR. *Journal of Non-Crystalline Solids* 2013, *368*, 17–22. https://doi.org/10.1016/j.jnoncrysol.2013.02.024.

[117] Sawyer, R.; Nesbitt, H. W.; Bancroft, G. M.; Thibault, Y.; Secco, R. A. Spectroscopic Studies of Oxygen Speciation in Potassium Silicate Glasses and Melts. *Canadian Journal of Chemistry* 2015, *93* (1), 60–73. https://doi.org/10.1139/cjc-2014-0248.

[118] Roy, B.; Rosin, A.; Gerdes, T.; Schafföner, S. Revealing the Surface Structural Cause of Scratch Formation on Soda-Lime-Silica Glass. *Sci Rep* 2022, *12* (1), 2681. https://doi.org/10.1038/s41598-022-06649-y.

[119] Morizet, Y.; Paris, M.; Hamon, J.; La, C.; Grolleau, S.; Suzuki-Muresan, T. Predicting Iodine Solubility at High Pressure in Borosilicate Nuclear Waste Glasses Using Optical Basicity: An Experimental Study. *J Mater Sci* 2022, *57* (35), 16600–16618. https://doi.org/10.1007/s10853-022-07686-8.